Available online at www.sciencedirect.com
ScienceDirect
Comput. Methods Appl. Mech. Engrg. 346 (2019) 642–673
Computer methods in applied mechanics and engineering
www.elsevier.com/locate/cma

Hybrid nearly singular integration for isogeometric boundary element analysis of coatings and other thin 2D structures

Yanpeng Gong[a,b], Jon Trevelyan[b], Gabriel Hattori[c], Chunying Dong[a,*]

[a] *Department of Mechanics, School of Aerospace Engineering, Beijing Institute of Technology, Beijing, 100081, China*
[b] *Department of Engineering, Durham University, Durham, DH1 3LE, UK*
[c] *Department of Engineering, University of Cambridge, Cambridge, CB2 1PZ, UK*

Received 17 August 2018; received in revised form 7 December 2018; accepted 8 December 2018
Available online 18 December 2018

Abstract

We present an isogeometric boundary element method (IGABEM) capable of delivering accurate and efficient solutions in the heat transfer analysis of 2D coated structures such as those commonly found in turbomachinery. Although we consider very thin coatings (of thickness down to 10^{-7} m), they are modelled explicitly as BEM zones, and this is made possible by the development of a new integration scheme ($\sinh^{+}$) aimed particularly at the challenging nearly singular integrals that arise. $\sinh^{+}$ is a hybrid of adaptive and sinh transformation approaches, and we make further extensions to the latter to improve its robustness. The scheme is tuned to deliver results of engineering accuracy in an optimal time. The scheme is adaptable, by changing a tolerance, to enable engineers to achieve a different balance between accuracy and computational efficiency as may be required for different applications. A set of numerical examples demonstrates the ability of the scheme to produce accurate temperature distributions efficiently in the presence of very thin coatings.

Keywords: Boundary element method; Isogeometric analysis; Nearly singular integrals; Coating structures

1. Introduction

The Boundary Element Method (BEM) is a standard numerical technique for the solution of partial differential equations, offering an alternative to the Finite Element Method (FEM) for a range of engineering simulations. Classically the BEM has been advantageous over the FEM for certain applications, including fracture mechanics and infinite domain problems such as acoustic and electromagnetic scattering. The advantages of the BEM derive from its boundary-only discretisation, the accuracy of its solutions on comparatively coarse meshes, and its ability to model discontinuous functions. The boundary-only discretisation suggests that the BEM should be most attractive for geometries having low surface area/volume ratios, and indeed the technique has been used very successfully in these cases. Although some specialised formulations have been proposed for shells, thin sections have historically presented challenges for practitioners working with the BEM. This largely results from the difficulty of integrating

* Corresponding author.
E-mail addresses: yanpenggong@gmail.com (Y. Gong), jon.trevelyan@durham.ac.uk (J. Trevelyan), gh465@cam.ac.uk (G. Hattori), cydong@bit.edu.cn (C. Dong).

https://doi.org/10.1016/j.cma.2018.12.019
0045-7825/

nearly-singular functions in a robust and computationally efficient manner in the assembly of the system matrix. In this paper we present a new scheme capable of producing accurate and efficient solutions for thin sections, focussing on coated structures, and this is made possible by the development of a new hybrid integration scheme for nearly singular integrals.

A comparatively recent development in the BEM literature is the move to isogeometric analysis with the BEM (i.e. the IGABEM). The isogeometric concept originated with Hughes et al. [1] who showed how, in an FEM context, there are significant benefits to be gained by replacing the piecewise polynomial approximation of the primary variable by an approximation formed in a basis of Non-Uniform Rational B-Spline (NURBS) functions. These benefits are: (i) the prospect for a much tighter integration of analysis and CAD modelling, (ii) the use of an exact geometric representation (i.e. the CAD geometry), (iii) the mesh refinement can be highly simplified using the standard knot-insertion and/or degree-elevation procedures, and (iv) the improved convergence properties of the solution over classical FEM. Not surprisingly, with these benefits, this initial work has attracted a large research community and the isogeometric concept expanded rapidly from elasticity [1,2] to other applications including fluid dynamics [3,4], electromagnetics [5], and vibration [6]. The initial works were based on NURBS [1], and then extended to T-splines [7], PHT-splines [8–10] and trimmed NURBS [11].

Since CAD and BEM both require only a boundary representation the linking of CAD geometries to the BEM in preference to the FEM seems a more natural choice. BEM analysis of 3D solids proceeds directly from a boundary representation, the most common geometric representation in CAD. Use of the IGAFEM to analyse a 3D solid presents challenges since it requires a volumetric NURBS description, which is not trivial to generate. There have been some early works injecting spline functions into the BEM, many of which predated the IGAFEM [12–18]. Simpson et al. [19,20] applied the isogeometric concept in a BEM framework, and found similar benefits over classical piecewise polynomial formulations. The IGABEM concept has been exploited in various areas including elastostatics [19,21,22], shape optimisation [23,24], acoustics [25–28], electromagnetics [29] and fracture mechanics [30]. The method is also amenable to BEM acceleration strategies, including Adaptive Cross Approximation [31,32] and the Fast Multipole Method [28,33].

However, the drawback of both BEM and IGABEM remains that the application to thin sections requires careful treatment. The current paper is motivated by the desire to extend the benefits of BEM, and more specifically IGABEM, to coated structures. These are commonly found in a wide range of engineering applications, but the focus of the current work is in turbomachinery, where a thermal barrier coating (TBC) is commonly applied to offer resistance to corrosion, wear and erosion and to enhance lubrication [34]. The coatings are, by definition, of small thickness. It is important for engineers to understand how the coating affects the thermal and stress distributions in these devices in order to design turbine systems which have the required durability.

When a thermal barrier coating is used to protect a turbine blade from corrosion, wear, and erosion, the coating thickness is typically 1 to 5 μm [34]. Therefore in the implementation of the isogeometric boundary element method on the coating zone, the distance r between the source point and field point will become very small, which will lead to complications in evaluating the boundary integrals required. Since the integrals contain fundamental solutions exhibiting $\ln r$ and $1/r$ behaviour, a large number of nearly singular integrals will arise while integrating over an element on the opposite side of the coating to the source point. In these cases, the required accuracy cannot be efficiently achieved using standard Gaussian quadrature. Without a carefully constructed integration scheme, problems containing thin materials such as coatings would require a very dense mesh making the BEM an unattractive option. There is therefore a considerable benefit to be derived from the development of accurate, efficient and robust schemes to evaluate nearly singular integrals so the benefits of BEM can be extended to these geometries.

Several techniques are available for the evaluation of nearly singular integrals in the conventional BEM. While analytical methods are feasible for simple cases [35], we focus on the approximate numerical and semi-analytical methods for generality of application in an IGABEM context. Telles [36] proposed a self-adaptive scheme that has become popular for the evaluation of weakly singular integrals in the BEM literature. This scheme was also shown to be an effective tool for the nearly-singular case. The method works by weakening the singularity of the integrand using a non-linear mapping of the integral interval from $[-1, 1]$ onto a new coordinate also in $[-1, 1]$. The method was extended by introducing a more efficient variable transformation in polar coordinates (referred to as the part method) [37]. Hayami [38] presented a new radial variable transformation for the part method, avoiding the need for analytical formulae, and undertook an error analysis using complex function theory. Sladek et al. [39] proposed a semi-analytical integration scheme to evaluate nearly singular integrals occurring in 2D BEM problems. Padhi

et al. [40] presented an analytical integration method for quadratic isoparametric boundary elements in which the distance function r^2 is expressed as a combination of polynomials $a+b\xi+c\xi^2+d\xi^3+e\xi^4$. Several semi-analytical or analytical methods have been used for elasticity problems [41–43] and potential problems [44]. In references [45–47], the line integral approach is used to transform nearly singular integrals into a sum of weakly singular integrals and regular line integrals, and this is applied in the analysis of thin-body problems. A simple and readily implemented method for interior field evaluations is introduced in [46], along with an auxiliary surface method, utilising the characters of the singular kernels. This method transforms nearly singular integrals on the original surface to integrals on an auxiliary surface. However, due to the use of the subdivision technique on the auxiliary surfaces, the method becomes inefficient. In [48], a parameterised Gaussian quadrature approach was presented to calculate the nearly singular integrals with kernels such as $\ln(\frac{1}{r})$, $\frac{1}{r}$ or $\frac{1}{r^2}$. In [49], the rigid body displacement solution is introduced to compute physical quantities near the boundary. The particular solution method is presented to compute stresses and displacements on and near boundaries in [50,51] and is then developed further to solve elastoplastic problems in [52]. In [53,54], an adaptive integral method is presented that is driven by the upper bound of the error estimate of Gauss quadrature along with an element subdivision technique. Because the number of Gauss points is chosen automatically, the method can compute nearly singular integrals to arbitrary accuracy. However, the method will be time-consuming where the distance from the source point to the field element becomes very small, especially for thin-body or coating structures.

Alternative methods based on regularisation are also available, including [55,56]. Luo et al. [57] combined the regularisation technique (singularity subtraction) and nonlinear transformation method to evaluate nearly singular integrals in 2D BEM in the solution of thin film problems for composite materials.

A simple method called the domain supplemental approach was presented by Ma [58] for avoiding the boundary layer effects encountered in solving problems of elasticity by the BEM. In [59] the approximate distance function was introduced to separate the near singular parts from the integrals with logarithmic kernels and to damp out the near singularities of the integrals with Cauchy and Hadamard kernels. Later a general algorithm called the distance transformation method was presented to evaluate nearly singular boundary integrals of various orders for elasticity problems [60]. In [61], a new implementation of the conventional distance scheme, which is redefined in two local coordinate systems, is given to stabilise the result. More recently, a spherical element subdivision method is presented by Zhang [62] to compute nearly singular integrals in 3D BEM.

In 2007, a non-linear coordinate transformation method called the sinh transformation method was presented in [63] for Laplace problems. The method is further developed in [64–70]. Similar to the sinh transformation method, an exponential transformation method has been widely used to cope with nearly singular integrals for the conventional BEM [68,71–73]. In [74], the exponential transformation method was applied to deal with the nearly singular integrals arising in IGABEM. The interested reader is directed to the works [68,74] for a full description of the method.

In this paper we present a new IGABEM formulation ($\sinh^+$) based on a hybrid integration scheme that combines the benefits of the sinh transformation (of, amongst others, Gu et al. [69]) and the adaptive integration scheme (of Gao et al. [54]). In order to enhance the robustness of the scheme, we further extend the sinh transformation by using the analytical extension of the NURBS curve to accommodate cases in which the projection of the source point lies outside the physical domain of the element.

An important requirement to be considered when developing an integration scheme for a BEM or FEM system is the balance between accuracy and computational efficiency. The requirement of most engineering FEM/BEM analyses is to deliver acceptable engineering accuracy with a small use of computational resources. However, the notion of 'acceptable engineering accuracy' can be expected to be interpreted differently by different engineers and for different applications. One valuable feature of the new $\sinh^+$ scheme is that, by changing a single tolerance parameter, engineers can tune the scheme to deliver the required accuracy for the problem at hand, without incurring the run-time cost of evaluating integrals to unnecessary precision. In this way the scheme is tuned to deliver engineering accuracy in the optimal computation time.

This paper is organised in the following sections. In Section 2 we provide an overview of the BEM and IGABEM formulation. In Section 3 we review existing methods for evaluating the nearly singular integrals that arise in a BEM analysis and undertake a detailed analysis of their accuracy and computational efficiency. In Section 4 we extend the sinh transformation with a new analytical extension approach that improves its robustness. Informed by the analysis in Section 3, we present in Section 5 our proposed $\sinh^+$ scheme. In Section 6 we demonstrate the effectiveness of the scheme through four numerical examples, and we close with some concluding remarks in Section 7.

2. Boundary element method and isogeometric boundary element method

2.1. Boundary integral equation

The Boundary Element Method (BEM) is a powerful tool for solving a range of engineering problems, in which the governing partial differential equation (PDE) is reformulated as a boundary integral equation allowing the computational model to be restricted to the boundary only. In the current paper, we apply the method to solve heat transfer problems, so that we seek the temperature field u and flux density in the domain Ω and on the boundary $\Gamma \equiv \partial\Omega$. In this paper we focus on 2D applications, so that $\Omega \subset \mathbb{R}^2$. The governing PDE is the Laplace equation

$$\nabla^2 u(\mathbf{x}) = 0, \quad \mathbf{x} \in \Omega \tag{1}$$

with normal flux density given by

$$q(\mathbf{y}) = -k\frac{\partial u(\mathbf{y})}{\partial n} \quad \mathbf{y} \in \Gamma, \tag{2}$$

where n is the unit outward pointing normal and k is the conductivity of the material. We solve (1) subject to a set of boundary conditions

$$u(\mathbf{y}) = \bar{u}, \quad \mathbf{y} \in \Gamma_D, \tag{3}$$

$$q(\mathbf{y}) = \bar{q}, \quad \mathbf{y} \in \Gamma_N, \tag{4}$$

$$q(\mathbf{y}) = h(u_a - u(\mathbf{y})), \quad \mathbf{y} \in \Gamma_R, \tag{5}$$

The known quantities $\bar{u}$ and $\bar{q}$ are prescribed temperatures and flux densities; Γ_D, Γ_N and Γ_R denote the Dirichlet, Neumann and Robin boundaries respectively, with $\Gamma_D \cup \Gamma_N \cup \Gamma_R = \Gamma$ and $\Gamma_D \cap \Gamma_N \cap \Gamma_R = \emptyset$; h denotes the (known) heat transfer coefficient, or film coefficient and u_a the (known) ambient temperature outside the material being analysed. For a 2D potential problem, the corresponding boundary integral equation can be written as

$$C(\mathbf{y})u(\mathbf{y}) + \int_\Gamma Q(\mathbf{y}, \mathbf{x})u(\mathbf{x})d\Gamma(\mathbf{x}) = \int_\Gamma U(\mathbf{y}, \mathbf{x})q(\mathbf{x})d\Gamma(\mathbf{x}), \quad \mathbf{y} \in \Gamma \tag{6}$$

Here $\mathbf{x} \in \Gamma$ and $\mathbf{y} \in \Gamma$ are commonly known as the field point and source point, respectively. $U(\mathbf{y}, \mathbf{x})$ and $Q(\mathbf{y}, \mathbf{x})$ denote the temperature and flux fundamental solution kernels, and $C(\mathbf{y})$ is the jump term that arises from the strongly singular nature of the integral of the flux kernel, so the integral on the left hand side of (6) should be interpreted in the Cauchy principal value sense.

The temperature and flux fundamental solution in 2D for isotropic materials are given as

$$U(\mathbf{y}, \mathbf{x}) = -\frac{1}{2\pi}\ln r, \tag{7}$$

$$Q(\mathbf{y}, \mathbf{x}) = \frac{\partial U}{\partial r}\frac{\partial r}{\partial \mathbf{n}(\mathbf{x})} = -\frac{1}{2\pi r}(r_{,1}n_1 + r_{,2}n_2), \tag{8}$$

where $r = r(\mathbf{y}, \mathbf{x}) = \|\mathbf{x}-\mathbf{y}\|$ is the distance between source point and field point, $r_{,i} = \frac{\partial r}{\partial x_i}$, and n_i is the ith component of the unit outward normal vector $\mathbf{n}$ to the boundary surface at the field point $\mathbf{x}$.

2.2. B-splines and NURBS basis

In this work, we focus our attention on methods of evaluating nearly singular integrals in the isogeometric boundary element method, which is a variant of the BEM based on the use of NURBS basis functions. Therefore, a brief introduction of B-splines and NURBS is given in this section. For the interested reader, a full description can be found in Piegl and Tiller [75].

A B-spline is defined using a group of piecewise polynomials, which are defined by the following "knot vector" of non-decreasing values

$$\Xi = \{\xi_1, \xi_2, \ldots, \xi_{n+p+1}\},\ \xi_a \in \mathbb{R}. \tag{9}$$

where a is the knot index, p the curve degree, and n the number of basis functions or control points $\mathbf{P}_a$. Each $\xi_a \in \Xi$ is called a knot. The B-spline basis functions of degree p are defined recursively; starting with $p = 0$ we define

$$N_{a,0}(\xi) = \begin{cases} 1, & \text{if } \xi_a \leq \xi < \xi_{a+1} \\ 0, & \text{otherwise,} \end{cases} \tag{10}$$

and, for $p = 1, 2, 3, \ldots$

$$N_{a,p}(\xi) = \frac{\xi - \xi_a}{\xi_{a+p} - \xi_a} N_{a,p-1}(\xi) + \frac{\xi_{a+p+1} - \xi}{\xi_{a+p+1} - \xi_{a+1}} N_{a+1,p-1}(\xi). \tag{11}$$

Thus, as is given in [75] a whole B-spline curve can be defined by n basis functions (in Eqs. (10) and (11)) and control points $\mathbf{P}_a$. But in the implementation of BEM, a discretised form of the boundary integral equation is commonly used, in which computations are focused on a single knot span, which corresponds to a single element in conventional BEM implementations. Therefore, in this work the descriptions of boundary geometry or physical quantities are given in a knot span with $p + 1$ non-zero basis functions, the values of which can be obtained by Eqs. (10) and (11).

A pth degree B-spline curve in a knot span (with $p+1$ non-zero basis functions) is constructed by a mapping from the parameter space to physical space, being

$$\mathbf{x}(\xi) = \sum_{a=1}^{p+1} N_{a,p}(\xi)\mathbf{P_a}, \tag{12}$$

where $\mathbf{P}_a$ denotes the set of control point coordinates and $\mathbf{x} = (x, y, z)$ is the location of the physical curve corresponding to the spatial coordinate ξ in parametric space.

NURBS, which are a dominant tool used to describe curves and surfaces in CAD systems, are developed from B-splines and can offer significant advantages due to their ability to describe circular arcs and other conic sections exactly. The NURBS geometry is a weighted form of the B-spline definition, i.e.

$$\mathbf{x}(\xi) = \sum_{a=1}^{p+1} R_{a,p}(\xi)\mathbf{P_a}, \tag{13}$$

where $R_{a,p}$ are the NURBS basis functions, which are defined by

$$R_{a,p}(\xi) = \frac{N_{a,p}(\xi)w_a}{W(\xi)} \tag{14}$$

with

$$W(\xi) = \sum_{a=1}^{p+1} N_{a,p}(\xi)w_a, \tag{15}$$

where a denotes the control point index, $N_{a,p}$ the B-spline basis function from (11), and w_a a weight associated with control point $\mathbf{P}_a$. When all of the weights are of equal value, the NURBS curve will degenerate to a B-spline curve.

At this point it is useful to emphasise that the control points do not all lie on the spline curve, and this will have implications addressed in the coming sections.

2.3. Isogeometric boundary element method implementation

Unlike the conventional BEM, in which the geometry and solution variables (temperature and flux density) are defined using C^0-continuous polynomial approximations, the isogeometric form (IGABEM) is characterised by the use of a spline basis to describe them, commonly B-splines or NURBS. In the implementation of IGABEM, the concept of an 'element' from the conventional BEM is considered as a knot span $[\xi_i, \xi_{i+1}]$, where $\xi_i, \xi_{i+1} \in \Xi$. The

boundary Γ may thus be considered to be divided into elements Γ_e, $e = 1, \ldots, N_e$. The temperature and flux density fields around the boundary are expressed using a NURBS expansion, i.e.

$$u(\xi) = \sum_{a=1}^{p+1} R_a(\xi)\tilde{u}_a, \tag{16}$$

$$q(\xi) = \sum_{a=1}^{p+1} R_a(\xi)\tilde{q}_a, \tag{17}$$

where $\tilde{u}_a$ and $\tilde{q}_a$ are the local temperature and flux parameters associated with the control point with index a. Readers familiar with the conventional BEM will notice that the shape functions have been replaced by NURBS basis functions. However, since the NURBS basis functions do not obey the Kronecker-Delta property, $\tilde{u}_a$ and $\tilde{q}_a$ should not be interpreted as the temperature and flux at control points (indeed, the control points may lie outside the material). Where control points are shared between adjacent elements, $\tilde{u}_a$ and $\tilde{q}_a$ apply to all elements to which the control point with index a belongs.

Replacing the continuous functions u and q by the expansions (16) and (17), the boundary integral equation (6) can be written in a discretised form:

$$C(\tilde{\zeta}_c)\sum_{a_0=1}^{p+1} R_{e_0a_0}(\tilde{\zeta}_c)\tilde{u}_{e_0a_0} + \sum_{e=1}^{N_e}\sum_{a=1}^{p+1} \mathrm{Q}_{ea}(\tilde{\zeta}_c, \tilde{\xi}_e)\tilde{u}_{ea} = \sum_{e=1}^{N_e}\sum_{a=1}^{p+1} \mathrm{U}_{ea}(\tilde{\zeta}_c, \tilde{\xi}_e)\tilde{q}_{ea} \tag{18}$$

where

$$\mathrm{Q}_{ea}(\tilde{\zeta}_c, \tilde{\xi}_e) = \int_{-1}^{1} Q(\tilde{\zeta}_c, \tilde{\xi}_e)R_{ea}(\tilde{\xi}_e)J_e(\tilde{\xi}_e)d\tilde{\xi}_e \tag{19}$$

$$\mathrm{U}_{ea}(\tilde{\zeta}_c, \tilde{\xi}_e) = \int_{-1}^{1} U(\tilde{\zeta}_c, \tilde{\xi}_e)R_{ea}(\tilde{\xi}_e)J_e(\tilde{\xi}_e)d\tilde{\xi}_e \tag{20}$$

c indicates the collocation point index, $\tilde{\zeta}_c$ the local coordinate of the collocation point, e_0 the element in which the collocation point is located, and a_0 is the local index of the collocation point in element e_0. e denotes the element index, $\tilde{\xi}_e$ is the local coordinate of the field point in its parent element, defined such that $\xi_e \in [-1, 1]$ in the element Γ_e, a is the local index of a basis function in element e, R_{ea} the corresponding basis function, and J_e the Jacobian. This may be computed simply using

$$J_e(\tilde{\xi}_e) = \frac{d\Gamma}{d\tilde{\xi}_e} = \frac{d\Gamma}{d\xi}\frac{d\xi}{d\tilde{\xi}_e} \tag{21}$$

Collocation of (18) taking the source point $\mathbf{y}$ at a sufficient number of locations (typically located at the Greville abscissae [76]), and application of the boundary conditions, leads to a linear system that may be solved for the temperature and flux density parameters $\tilde{u}_a$ and $\tilde{q}_a$. The temperature and flux density fields on Γ may then be recovered from (16) and (17). Where the problem consists of two or more different materials, the standard techniques for multizone BEM [77] may be adopted without change for the IGABEM.

3. Analysis of existing methods for the evaluation of nearly singular boundary integrals

3.1. Adaptive integral method

A standard Gauss quadrature formula can be expressed by the following equation

$$I = \int_{-1}^{1} F(\xi)d\xi = \sum_{i=1}^{m} wF(\xi) + E. \tag{22}$$

where w is the weight factor, m is the number of Gauss points, and E is the integration error. The upper bound of relative error $\bar{e}$ can be approximated by [78]

$$\frac{E}{I} \leq 2\left(\frac{L}{4d}\right)^{2m}\frac{(2m+\beta-1)!}{(2m)!(\beta-1)!} \leq \bar{e} \tag{23}$$

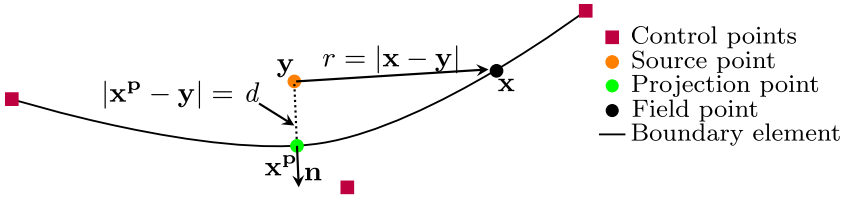

Fig. 1. Minimum distance d to the element when $\mathbf{x}^p \in \Gamma_e$.

where β is the order of singularity (i.e. the integrand is of the form $r^{-\beta}$), L is the length of the element, and d is the minimum distance from the source point to the element.

According to [53,54,79], the following equation can be obtained

$$m = \sqrt{\frac{2}{3}\beta + \frac{2}{5}}\left[-\frac{1}{10}\ln\left(\frac{\bar{e}}{2}\right)\right]\left[\left(\frac{8L}{3d}\right)^{3/4} + 1\right] \tag{24}$$

which can be rearranged to yield

$$L = \frac{3}{8}d\left(\frac{-10m}{\sqrt{2\beta/3 + 2/5}\ln(\bar{e}/2)} - 1\right)^{3/4} \tag{25}$$

giving the length of an element over which a given Gauss order can deliver a prescribed accuracy.

Based on the above analysis, and introducing an element subdivision algorithm, Gao and Davies presented the adaptive integration method in [53,54], giving details of the derivation and implementation for the conventional BEM. The implementation of the adaptive integral method in IGABEM can be found in [80,81].

In the process of integral evaluation, to avoid using high Gauss order m, the element should be repeatedly divided into sub-elements which reduces the ratio $\frac{L}{d}$. In this way, nearly singular integrals can be accurately computed using moderate Gauss orders by controlling the ratio $\frac{L}{d}$. However, one drawback of the method is that large numbers of sub-elements will be produced for the more extreme near-singularities, so a large number of Gauss point evaluations are still required. This can be a problem for coating structures.

3.2. Sinh transformation method

The sinh transformation method has been demonstrated to be feasible in dealing with the nearly singular integrals in the conventional BEM [66,67,69,82–84]. The current Section 3.2 largely follows these works, however we adapt the method to the IGABEM context. The scheme has been applied to IGABEM for Helmholtz problems [85], however no results for individual integrals were reported and the current authors have been unable to achieve the required accuracy with their own implementation of [85] for the Laplace problem. In the following, we will develop the sinh transformation method for the nearly singular integrals that arise in IGABEM.

Consider one general isogeometric boundary Γ_e with knot span $[\xi_i, \xi_{i+1}]$ as shown in Fig. 1. The minimum distance d from the source point (computed point) to the integration element Γ_e is defined as $|\mathbf{x}^p - \mathbf{y}|$, where $\mathbf{x}^p$ is the projection point of $\mathbf{y}$ onto the integration element Γ_e. It is noted that in the case depicted in Fig. 1, $\mathbf{x}^p$ is on Γ_e, i.e. $\mathbf{x}^p \in \Gamma_e$. The case in which $\mathbf{x}^p \notin \Gamma_e$ will be introduced in the next section. Let ξ_p (with $\xi_i \leq \xi_p \leq \xi_{i+1}$) be the local intrinsic coordinate of the projection point $\mathbf{x}^p$, i.e. $\mathbf{x}^p = (x_1(\xi_p), x_2(\xi_p))$.

To determine the minimum distance d and local intrinsic coordinates of ξ_p, a Newton–Raphson iterative scheme was proposed in [53]. The method is also used in the adaptive integral method for computing the minimum distance from source point to sub-element. More details about the Newton–Raphson method for the conventional BEM can be found in [53], and the application for IGABEM has been given in [81].

As shown in Fig. 1, the minimum distance d from the source point to the integration element is defined as perpendicular to the tangential line, through the computed point and projection point. We recall that the field point $\mathbf{x}$ can be described as a rational polynomial with respect to ξ by (13).

By applying the Taylor's expansion of $\mathbf{x}(\xi)$ in the neighbourhood of projection point $\mathbf{x}^p(\xi_p)$ in parameter space, formulae of the following form can be established:

$$\begin{aligned} x_k - y_k &= x_k - x_k^p + x_k^p - y_k \\ &= (x_k^p - y_k) + \left.\frac{dx_k}{d\xi}\right|_{\xi=\xi_p}(\xi-\xi_p) + \left.\frac{1}{2}\frac{d^2x_k}{d\xi^2}\right|_{\xi=\xi_p}(\xi-\xi_p)^2 + \cdots \\ &+ \left.\frac{1}{n!}\frac{d^nx_k}{d\xi^n}\right|_{\xi=\xi_p}(\xi-\xi_p)^n + \text{HOT} \end{aligned} \tag{26}$$

where $k = 1, 2$, $\mathbf{x} = (x_1, x_2)$, $\mathbf{y} = (y_1, y_2)$, $\mathbf{x}^p = (x_1^p, x_2^p)$, n is the order of Taylor expansion and HOT abbreviates Higher Order Terms. The derivatives are found from

$$\frac{d^n x_k}{d\xi^n} = \sum_{i=1}^{p+1} \frac{d^n}{d\xi^n} R_{i,p}(\xi)\mathbf{P}_{ik} \tag{27}$$

where $\mathbf{P}_{ik}$ is the k coordinate of the ith control point. The first order derivative of a NURBS basis function is expressed as [20]

$$\frac{d}{d\xi}R_{i,p}(\xi) = \omega_i \frac{W(\xi)N'_{i,p}(\xi) - W'(\xi)N_{i,p}(\xi)}{(W(\xi))^2} \tag{28}$$

where $N_{i,p}(\xi)$ is the B-spline basis function given in Eqs. (10) and (11), $N'_{i,p}(\xi) = \frac{d}{d\xi}N_{i,p}(\xi)$, and $W'(\xi) = \sum_{j=1}^{n} N'_{j,p}(\xi)\omega_j$.

The higher-order derivatives of the rational function can be expressed in terms of lower-order derivatives as [20]

$$\frac{d^k}{d\xi^k}R_{i,p}(\xi) = \frac{A_i^{(k)}(\xi) - \sum_{b=1}^{k}\binom{k}{b}W^{(b)}(\xi)\frac{d^{(k-b)}}{d\xi^{(k-b)}}R_{i,p}(\xi)}{W(\xi)} \tag{29}$$

where $\binom{k}{b} = \frac{k!}{b!(k-b)!}$, $A_i^{(k)}(\xi) = \omega_i \frac{d^k}{d\xi^k}N_{i,p}(\xi)$ and $W^{(b)}(\xi) = \frac{d^b}{d\xi^b}W(\xi)$.

From Fig. 1, the following relation can be obtained

$$\mathbf{x}_k^p - \mathbf{y}_k = dn_k(\xi_p), \tag{30}$$

where n_k indicates the component of the unit outward normal of the boundary.

For brevity, let

$$D_{k,\xi}^n = \left.\frac{1}{n!}\frac{d^nx_k}{d\xi^n}\right|_{\xi=\xi_p} \tag{31}$$

From Eqs. (30) and (31), the expansion (26) can be rewritten as

$$x_k - y_k = dn_k(\xi_p) + D_{k,\xi}^1(\xi-\xi_p) + D_{k,\xi}^2(\xi-\xi_p)^2 + \cdots + D_{k,\xi}^n(\xi-\xi_p)^n + \text{HOT} \tag{32}$$

Invoking the relation $n_k D_{k,\xi}^1 = 0$, then, the square of the distance between the source point and the field point, i.e. r^2, can be expressed as

$$\begin{aligned} r^2(\xi) &= (x_1 - y_1, x_2 - y_2)\cdot(x_1 - y_1, x_2 - y_2) \\ &= d^2 + (\xi-\xi_p)^2 g_n(\xi) + E_{\text{trun}} \end{aligned} \tag{33}$$

where $d = |\mathbf{x}^p - \mathbf{y}|$ is the minimum distance (shown in Fig. 1), n is the order of the Taylor expansion, and $g_n(\xi)$ is a function containing sums of products of terms in the Taylor expansion. E_{trun} is the truncation error arising from neglecting the higher order terms in the approximation. Substituting Eq. (33) into the boundary integrals in Eq. (6) yields the following integral:

$$I_1 = \int_{\xi_i}^{\xi_{i+1}} f(\xi)\ln r^2 d\xi = \int_{\xi_i}^{\xi_{i+1}} f(\xi)\ln\left(d^2 + (\xi-\xi_p)g_n(\xi) + E_{\text{trun}}\right)d\xi \tag{34}$$

$$I_2 = \int_{\xi_i}^{\xi_{i+1}} \frac{f(\xi)}{r^2}d\xi = \int_{\xi_i}^{\xi_{i+1}} \frac{f(\xi)}{d^2 + (\xi-\xi_p)g_n(\xi) + E_{\text{trun}}}d\xi \tag{35}$$

In order to correctly represent the behaviour of the kernels, the term $f(\xi)$ in (34) needs to include a factor of 0.5 (since $\ln r = 0.5 \ln r^2$) and the term $f(\xi)$ in (35) needs to include a factor of r (since $1/r = r/r^2$). Unlike the conventional BEM with polynomial interpolation function (i.e. Lagrange interpolation basis), the higher-order derivatives of the NURBS basis functions will not vanish (as shown in Eq. (32)). Therefore, the term E_{trun} in (33) cannot be ignored. Clearly, the higher the order of the Taylor series in (32), the smaller will be the error E_{trun}. In this paper, we will develop a method to keep the error E_{trun} within acceptable limits.

In the following work, the nearly singular integrals in Eqs. (34) and (35) over an isogeometric element Γ_e with knot span $[\xi_i, \xi_{i+1}]$ will be analysed and a general method for their computation will be given. Firstly, the knot span should be split into two sub-knot spans $[\xi_i, \xi_p]$ and $[\xi_p, \xi_{i+1}]$ at the projection point $\mathbf{x}^p$, so that the integrals (34) and (35) are expressed

$$I_1 = \int_{\xi_i}^{\xi_p} f(\xi) \ln r^2 d\xi + \int_{\xi_p}^{\xi_{i+1}} f(\xi) \ln r^2 d\xi \tag{36}$$

$$I_2 = \int_{\xi_i}^{\xi_p} \frac{f(\xi)}{r^2} d\xi + \int_{\xi_p}^{\xi_{i+1}} \frac{f(\xi)}{r^2} d\xi \tag{37}$$

where $r^2 = d^2 + (\xi - \xi_p)^2 g_n(\xi) + E_{\text{trun}}$. The integrals above should be computed separately on each sub knot span. Here, for brevity and without loss of generality, only the following integral with knot span $[\xi_i, \xi_p]$ in Eq. (37) is considered

$$\int_{\xi_i}^{\xi_p} \frac{f(\xi)}{d^2 + (\xi - \xi_p)^2 g_n(\xi) + E_{\text{trun}}} d\xi \tag{38}$$

Similar procedures can be developed for the other integrals.

We proceed by defining a nonlinear coordinate transformation mapping $s \in [-1, 1]$ to the parametric coordinate $\xi \in [\xi_i, \xi_p]$, using

$$\xi = \xi_p + d \ \sinh[a(s-1)] \tag{39}$$

where

$$a = \frac{1}{2} \text{arcsinh}\left(\frac{\xi_p - \xi_i}{d}\right) \tag{40}$$

The Jacobian of transformation is given by

$$J = \frac{d\xi}{ds} = d\, a \ \cosh[a(s-1)] \tag{41}$$

After the transformation the squared distance r^2 can be written as

$$r^2 = d^2 \left(1 + \sinh^2[a(s-1)] g_n(s)\right) + E_{\text{trun}} \tag{42}$$

Substitution of the sinh transformation (39) and transformed distance function (42) into the nearly singular integral (38), yields

$$\frac{1}{d} \int_{-1}^{1} \frac{a \cosh[a(s-1)] f(s)}{1 + \sinh^2[a(s-1)] g_n(s) + E_{\text{trun}}} ds \tag{43}$$

By following the above procedure, the near singularity of the integrand on the knot span has been fully regularised, and the integral can be evaluated directly by standard Gauss–Legendre quadrature.

3.3. Error analysis

3.3.1. Line isogeometric element

In this section we will compare the relative error of several methods outlined above. Firstly, a simple line isogeometric element is considered, as shown in Fig. 2(a). The element is represented as a quadratic NURBS curve with knot vector $\Xi = \{0, 0, 0, 1, 1, 1\}$, control points $P_1 = (0, 0)$, $P_2 = (0.5, 0)$ and $P_3 = (1, 0)$ and weights $[1, 1, 1]$. The location of the source point is chosen as $\mathbf{y} = (0.5, d)$, in which d is the distance from the source point to the

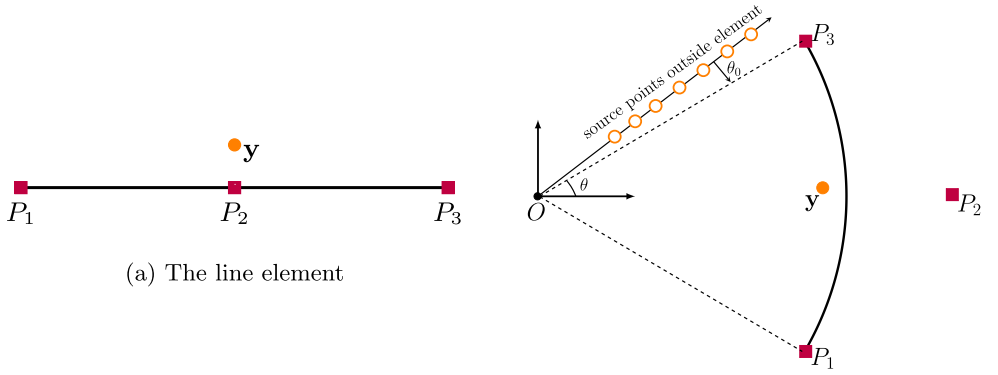

(a) The line element

(b) The arc element

Fig. 2. Considered isogeometric elements.

element; in this study d varies from around 1 to 0.0000001. We introduce the dimensionless aspect ratio $d^* = d/L$ to describe the proximity of the source point to the element, where L denotes the length of the element. Since the source point is close to the element, the integrals (19) and (20) will be nearly singular. Where the kernel in the integral has a strong singularity, i.e. (19), we call this a strong nearly singular integral, and similarly where the kernel has a weak singularity, i.e. (20), we call this a weak nearly singular integral. We present here the relative errors, ε_r, in evaluating both cases, where

$$\varepsilon_r = \left| \frac{I_{\text{num}} - I_{\text{ref}}}{I_{\text{ref}}} \right| \tag{44}$$

where I_{num} and I_{ref} denote the numerical and reference values of the considered integral, respectively. The reference solutions for integrals considered in Sections 4 and 3.3 are found numerically using the Matlab function 'int' to convergence.

Fig. 3 shows the relative error in evaluating the weak nearly singular integral by different methods as the source point approaches the element. In the computation, 8 Gauss points are used to evaluate each integral. For evaluations using the adaptive scheme, an upper bound relative error $\bar{e} = 10^{-8}$ is taken. When the source point is not very close to the boundary, i.e. $d^* > 0.5$, all the considered methods can be seen to yield accurate results. However, with the decrease of the aspect ratio d^*, the performance of conventional Gaussian quadrature is less satisfactory. From Fig. 3, it can be seen that (for the same number of Gauss points) the Telles scheme outperforms standard Gauss–Legendre, but for small d^* it is unable to deliver a relative error below about 0.01 for the weak nearly singular integral with 8 Gauss points. In contrast, the relative errors of the adaptive method, the sinh transformation method and the exponential method remain below 10^{-5} even when the aspect ratio d^* becomes very small. Fig. 4 shows the relative error of the strong nearly singular integral evaluation by different methods as the source point approaches the element. For this strongly singular integrand, 25 Gauss points are used for the evaluations. It can be clearly seen from the figure that all the considered methods can produce accurate results when the aspect ratio $d^* > 0.5$. However, when $d^* < 0.5$, the results obtained by the Gauss–Legendre quadrature and Telles methods become less satisfactory. We remark that we are applying the Telles scheme here to an integrand of higher order singularity than is strictly appropriate, but since this is a nearly singular (not singular) integral, the transformation remains an improvement over an unmodified Gauss–Legendre scheme. The exponential transformation method, the sinh transformation method and the adaptive integral method are still able to deliver high accuracy even when the aspect ratio $d^* = 10^{-7}$. One can also see that the adaptive integral method is emerging as the most accurate approach of those tested, with a relative error ε_r remaining around 10^{-7} and being two to three orders of magnitude smaller than ε_r found with the exponential transformation and sinh transformation methods.

3.3.2. Arc isogeometric element

The arc isogeometric element given in Fig. 2(b) is also represented as a quadratic NURBS curve with knot vector $\Xi = \{0, 0, 0, 1, 1, 1\}$, control points $P_1 = \left(\cos(-\frac{\pi}{6}), \sin(-\frac{\pi}{6})\right)$, $P_2 = (1.155, 0)$, $P_3 = \left(\cos(\frac{\pi}{6}), \sin(\frac{\pi}{6})\right)$ and weights

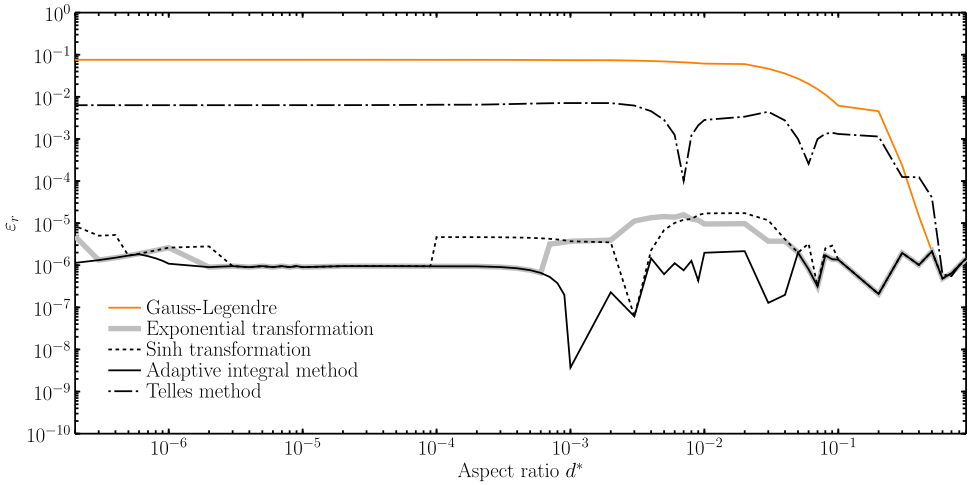

Fig. 3. Relative errors obtained by different methods for weak nearly singular integral on line isogeometric element.

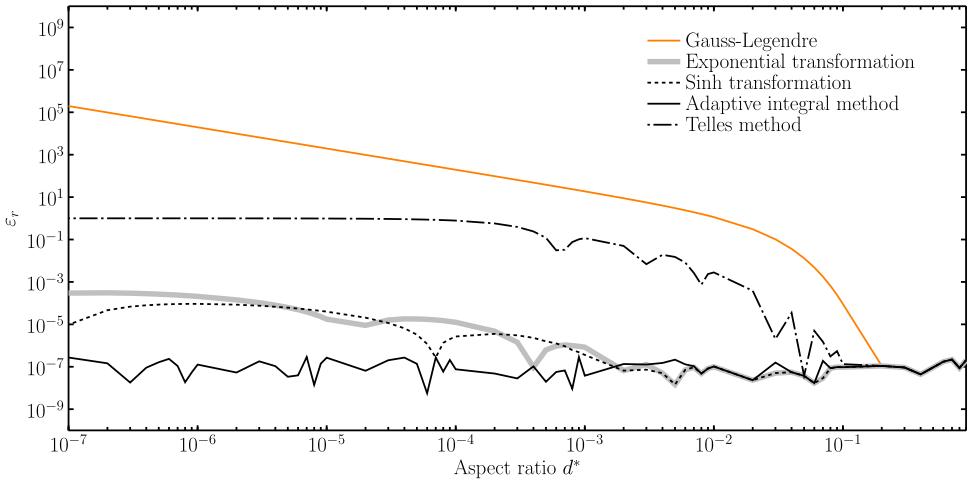

Fig. 4. Relative errors obtained by different methods for strong nearly singular integral on line isogeometric element.

[1, 0.866025, 1]. The source point **y** is close to the element with coordinates $(1 - d, 0)$, where d denotes the distance from **y** to the element; in this study we consider d in the range 1 to 10^{-7}.

Figs. 5 and 6 show the results of weak and strong nearly singular integral evaluations by different methods when the source point approaches the boundary element. Similar to the line element tests, 8 Gauss points are used for the weak nearly singular integral and 25 Gauss points are used for the strong nearly singular integral. One can see that similar conclusions as for the line element can be drawn. The adaptive method can obtain highly accurate evaluations of both weak and strong nearly singular integrals. From Fig. 5, it is evident that the relative errors of the sinh and exponential transformations start to grow for $d^* > 10^{-4}$, but the accuracy remains quite satisfactory down to $d^* < 10^{-7}$ for most practical engineering problems. These errors are strongly driven by the number of Gauss points used; it is clear that the relative errors for the sinh and exponential transformations are markedly reduced when 25 Gauss points are used, even for the higher order singularity in the kernel, as shown in Fig. 6. Figs. 7(a), 7(b), 8(a) and 8(b) give a set of results showing how the errors in sinh and exponential transformations change when different numbers of Gauss points are used.

From the above comparisons, the adaptive integral method, sinh transformation method and exponential transformation methods can achieve satisfactory results in the computation of nearly singular integrals. The adaptive integral

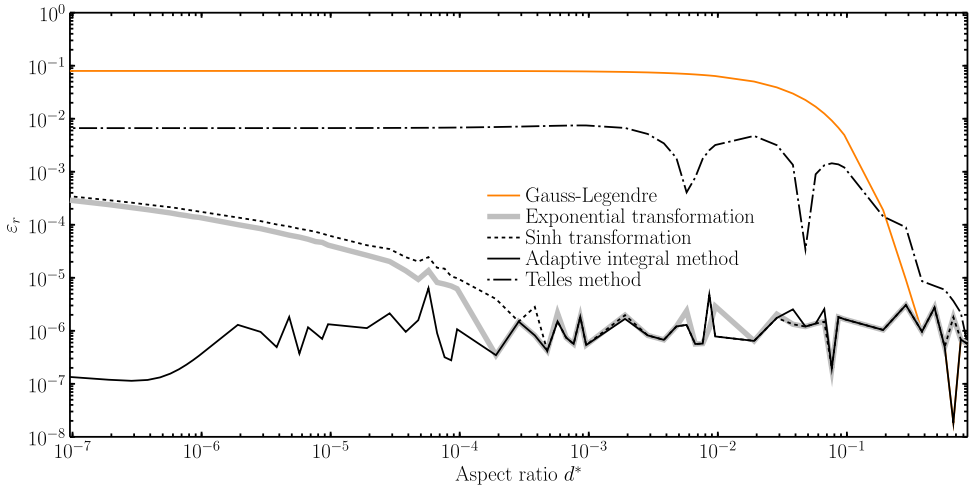

Fig. 5. Relative errors obtained by different methods for weak nearly singular integral on arc isogeometric element.

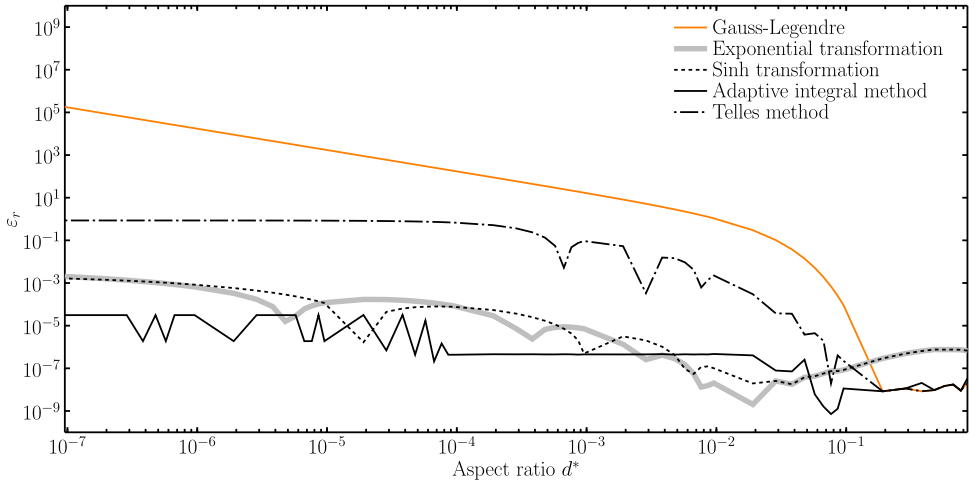

Fig. 6. Relative errors obtained by different methods for strong nearly singular integral on arc isogeometric element.

method can consistently deliver very high accuracy although both the sinh and exponential transformation methods can obtain satisfactory results.

3.4. Efficiency analysis

Efficiency is another key metric for the evaluation of a numerical method. The aim in an engineering context is often to achieve results of acceptable accuracy in as short a time as possible with the available resources. Sometimes, engineers may find it beneficial to reduce the accuracy of an algorithm to improve the computational efficiency, as long as the accuracy remains acceptable. It is clear that the different integration schemes offer different degrees of accuracy, so we now investigate their computational efficiency.

The error analysis suggests that we proceed focussing on the adaptive method and the sinh transformation as the two preferred schemes. The elements in Figs. 2(a) and 2(b) and the nearly singular integrals in Eqs. (19) and (20) are considered for further study. As in the error analysis, we retain the use of 8 and 25 Gauss points for the evaluations of the integrals containing the weakly and strongly singular kernels, respectively. It is for this reason that, when we plot the CPU time requirements in Figs. 9(a), 9(b) and 10(a), 10(b), the evaluation of the strong nearly singular integral

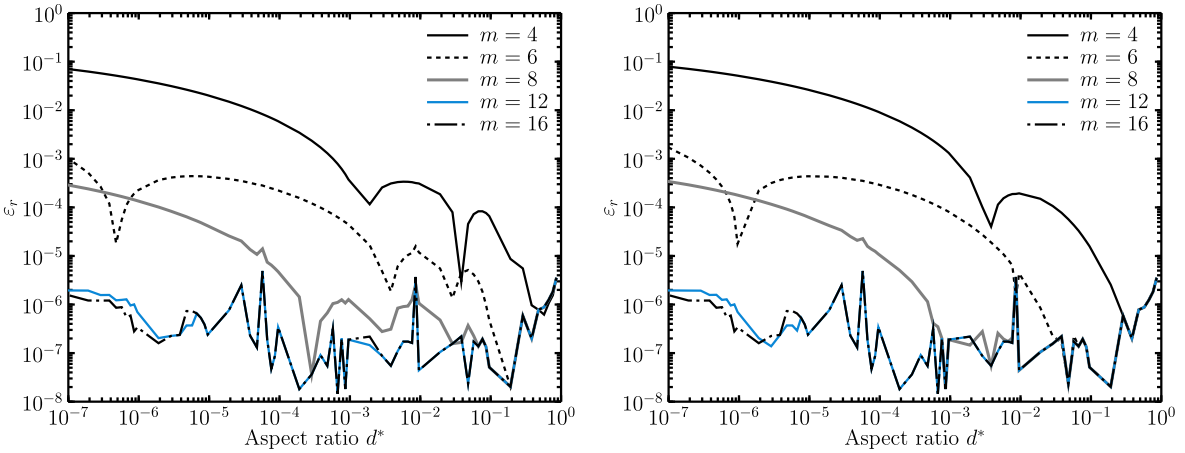

(a) Errors of exponential transformation

(b) Errors of sinh transformation

Fig. 7. Errors of exponential and sinh transformations change when different numbers of Gauss points are used for the weak nearly singular integral.

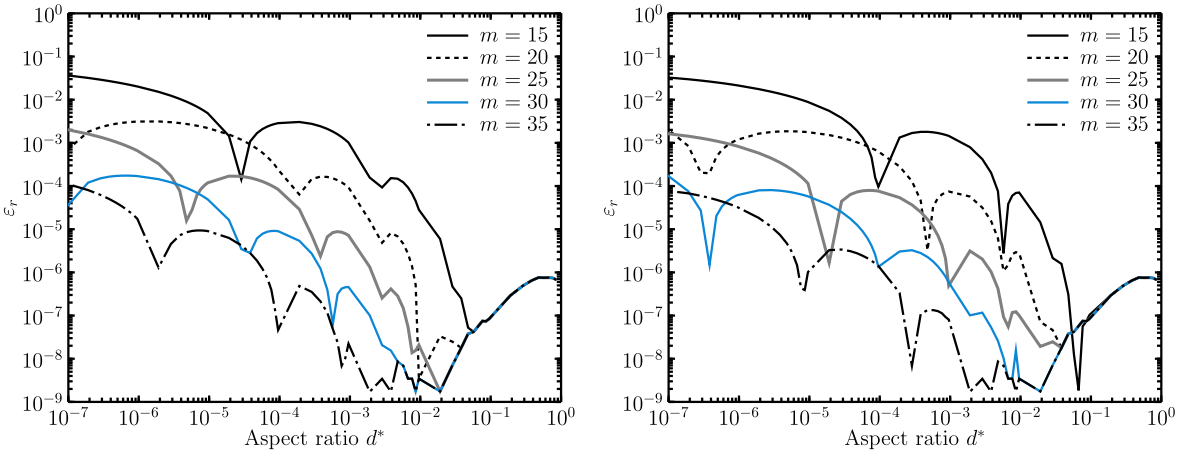

(a) Errors of exponential transformation

(b) Errors of sinh transformation

Fig. 8. Errors of exponential and sinh transformations change when different numbers of Gauss points are used for the strong nearly singular integral.

using the sinh transformation takes approximately three times more time than that of the weak nearly singular integral. The adaptive scheme CPU time is plotted for different error tolerances $\overline{e} = 10^{-6}, 10^{-8}, 10^{-10}$. There is little visual difference in the CPU time for these three tolerances; although this can be partially attributed to the compression arising from the use of a log scale, it should be remembered that the scheme will create very small subdivisions only locally around the source point, while larger regions of the element are integrated using the same discretisation. In order to illustrate this point, the total number of sub-elements and Gauss points used in the adaptive method for strong nearly singular integrals with $\overline{e} = 10^{-6}, 10^{-8}, 10^{-10}$ is given in Table 1. It is evident that, for small d^*, each reduction of two orders of magnitude in $\overline{e}$ results in an increase of only about 10% in the number of sub-elements and Gauss points. This confirms the reason that the lines showing the CPU time for the adaptive scheme in Figs. 9(a), 9(b) and 10(a), 10(b) are so close together.

The significant feature of these figures is the point at which the sets of lines for the different schemes cross. This shows that the adaptive scheme will be the more efficient for aspect ratios $d^* \geq 0.07$ for the weak nearly singular integral, and for aspect ratios $d^* \geq 0.03$ for the strong nearly singular integrals. For smaller d^* the sinh transformation

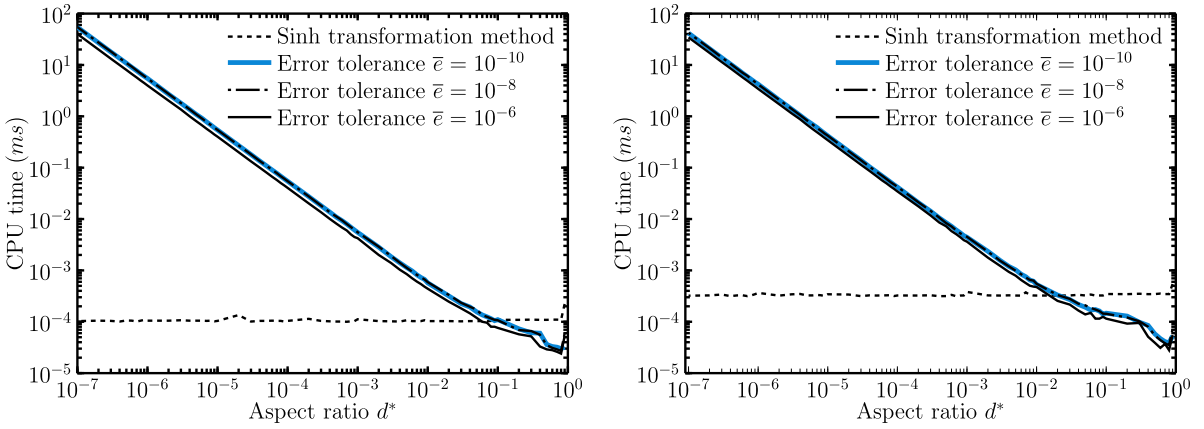

(a) Weak nearly singular integral

(b) Strong nearly singular integral

Fig. 9. CPU time comparison between adaptive integral method and sinh transformation method on isogeometric line element.

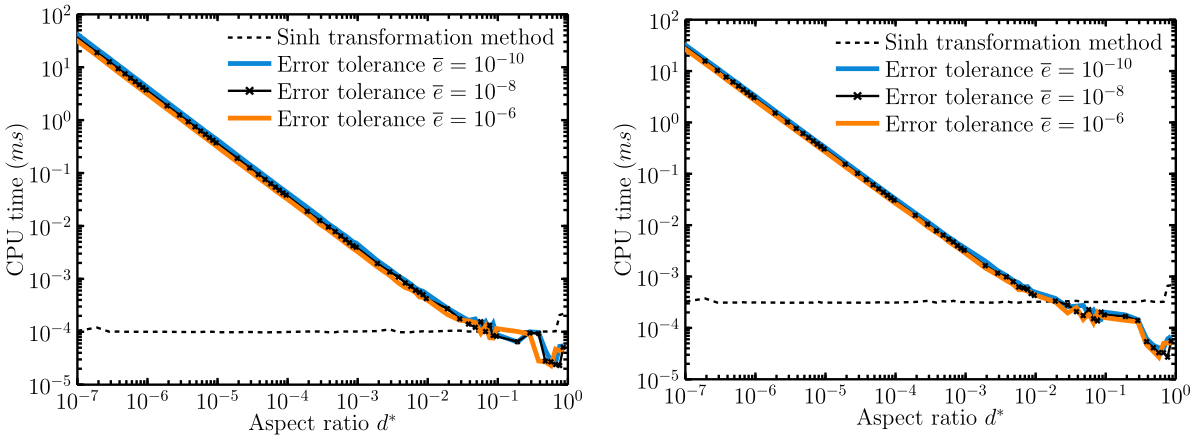

(a) Weak nearly singular integral

(b) Strong nearly singular integral

Fig. 10. CPU time comparison between adaptive integral method and sinh transformation method on isogeometric arc element.

will be the more efficient scheme. This conclusion is summarised in Table 2, in which we introduce the notation d^*_{crit} for this critical aspect ratio. While direct comparison is not appropriate because of the different accuracies considered, Figs. 9(a), 9(b), 10(a) and 10(b) provide the basis for a quantification of d^*_{crit} as listed in Table 2.

4. Extended sinh transformation

In Section 3.2, the sinh transformation was presented for the case in which the projection point lies in the element, i.e. $\mathbf{x}^p \in \Gamma_e$. However, we must note that in a practical engineering simulation, many cases can arise in which the source point lies close to one end of the element in such a way that the projection point lies outside the element. Such a case is illustrated in Fig. 11, and here we denote the projection point $\mathbf{x}^{p'}$ to emphasise that $\mathbf{x}^{p'} \notin \Gamma_e$. In the current work we assume $\mathbf{x}^{p'}$ to lie close to the end of the element, as it will be shown that this scheme will be applied only for small d^*. In order to develop a robust integration scheme, we present a new adaptation of the sinh transformation approach based on the analytical extension of the NURBS curve.

Here, we take the arc element in Fig. 2(b) as an example. For the development of the method, and without loss of generality, we consider the knot span of the element to be [0, 1]. For a NURBS curve of degree $p = 2$, the basis functions $R_{a,p}$, $a = 1, 2, 3$ are plotted in Fig. 12(a).

Table 1
Total number of sub-elements and Gauss points used in the adaptive method for strong nearly singular integrals on arc element.

Error tolerance e_i	10^{-6}		10^{-8}		10^{-10}	
Aspect ratio d^*	No. SE	No. GP	No. SE	No. GP	No. SE	No. GP
6.68×10^{-1}	1	6	1	9	1	11
5.73×10^{-1}	1	7	1	10	1	13
4.77×10^{-1}	1	9	1	13	1	16
3.82×10^{-1}	1	14	1	18	1	22
2.86×10^{-1}	2	14	2	20	2	26
1.91×10^{-1}	2	28	2	36	2	44
9.55×10^{-2}	4	36	4	48	4	60
9.55×10^{-3}	32	114	35	122	39	156
9.55×10^{-4}	317	670	349	750	384	852
9.55×10^{-5}	3168	6386	3484	7030	3832	7748
9.55×10^{-6}	31 675	63 386	34 835	69 723	38 312	76 682
9.55×10^{-7}	316 742	633 498	348 351	696 742	383 115	766 292

Note: 'No. SE' stands 'number of sub-elements'; 'No. GP' indicates 'number of Gauss points'.

Table 2
Efficient method for different nearly singular integrals.

Aspect ratio	Weak nearly singular integral		Strong nearly singular integral	
	$d^* < d^*_{crit} = 0.07$	$d^* \geq d^*_{crit} = 0.07$	$d^* < d^*_{crit} = 0.03$	$d^* \geq d^*_{crit} = 0.03$
Efficient method	Sinh transformation	Adaptive integral	Sinh transformation	Adaptive integral

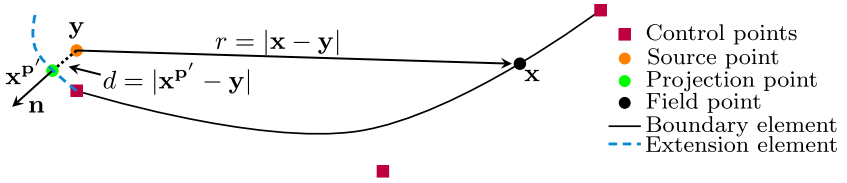

Fig. 11. Minimum distance d to the extension element when $\mathbf{x}^{p'} \notin \Gamma_e$.

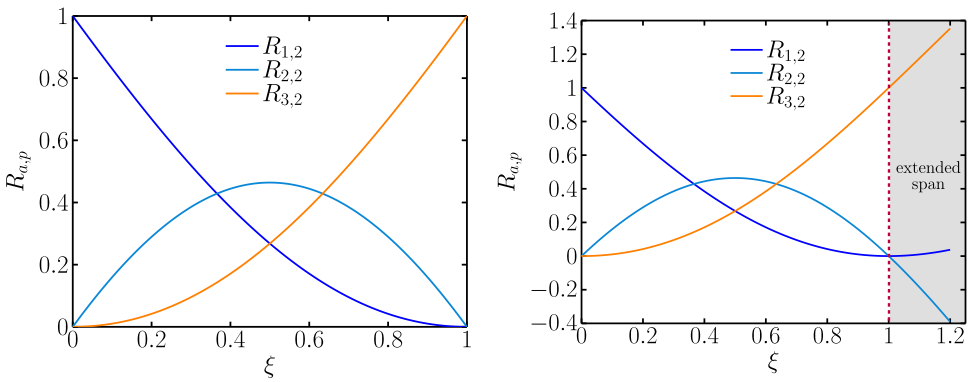

(a) Normal NURBS basis functions

(b) Extended NURBS basis functions

Fig. 12. NURBS basis functions of the considered isogeometric element.

Since the NURBS basis functions are a set of continuous functions of ξ, we can apply them to values of ξ outside the knot span of the element. For example Fig. 12(b) shows the same NURBS functions applied to $\xi \in [0, 1.2]$. This analytical extension is non-physical and not intended to describe the component geometry. This allows us to apply the sinh transformation where the parameter $\xi_{p'}$ of the projection point $\mathbf{x}^{p'}$ will lie in the extended span (grey zone) of

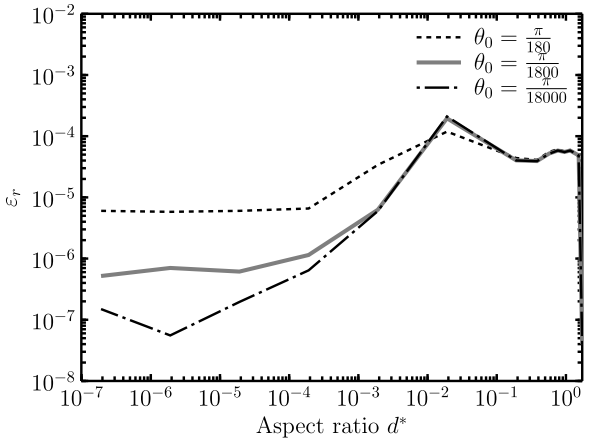

Fig. 13. Relative errors obtained by extended sinh transformation for strong nearly singular integral on arc isogeometric element.

Fig. 12(b). The expanded curve (both the dashed curve and solid curve in Fig. 11) can be expressed by

$$\mathbf{x}(\xi) = \sum_{a=1}^{p+1} R_{a,p}(\xi)\mathbf{P}_\mathbf{a}, \quad \xi \in \left[0, \xi^{p'}\right], \quad \xi^{p'} > 1 \tag{45}$$

A similar expression can be written for cases in which the projection point is just outside the other end of the element, i.e. for the case $\xi^{p'} < 0$.

Considering the extended isogeometric element, the distance $d = |\mathbf{y} - \mathbf{x}^{p'}|$ will be the perpendicular distance from the source point to the projection point which may be located in the analytically extended part of the element. The projection point and corresponding distance d can be found using the identical Newton–Raphson scheme as before. Therefore, Eqs. (30) and (33) still apply. However, for this case, the nearly singular integrals (36) and (37) will become

$$I_1 = \int_{\xi_i}^{\xi_{p'}} f(\xi) \ln r^2 d\xi - \int_{\xi_{i+1}}^{\xi_{p'}} f(\xi) \ln r^2 d\xi \tag{46}$$

$$I_2 = \int_{\xi_i}^{\xi_{p'}} \frac{f(\xi)}{r^2} d\xi - \int_{\xi_{i+1}}^{\xi_{p'}} \frac{f(\xi)}{r^2} d\xi \tag{47}$$

with similar expressions for the case $\xi^{p'} < 0$.

To illustrate the accuracy of the extended sinh transformation, Fig. 13 shows the relative errors in the evaluation of the strong nearly singular integral over the arc isogeometric element with source points located outside the subtended arc of the element, as shown in Figs. 11 and 2(b). The position of the source point is described by

$$x = r\cos(\theta + \theta_0);\ y = r\sin(\theta + \theta_0). \tag{48}$$

We consider r varying from 0.1 to 0.9999999 (the circle has unit radius), $\theta = \frac{\pi}{6}$, and angle $\theta_0 = (\frac{\pi}{180}, \frac{\pi}{1800}, \frac{\pi}{18000})$ is a small angle, as shown in Fig. 2(b). These results demonstrate that the extended sinh transformation can obtain very accurate results, even when the source point is very close to the element and the projection point lies outside the element.

5. Hybrid integration scheme

As discussed in Sections 3.3 and 3.4, both the error and efficiency of the considered computation methods are related to the aspect ratio d^*, which describes the proximity of the source point to the element. The conclusion drawn from these sections is that a satisfactory balance between accuracy and efficiency cannot be achieved simultaneously by using only one of the considered methods (sinh transformation method or adaptive method). In Section 3.4 we identify a critical value d^*_{crit}, quantified in Table 2, that can be used to inform a hybrid approach using the best

features of both. When the aspect ratio $d^* > d^*_{crit}$, there is no near-singularity and the adaptive integration method is applied. However, for $d^* < d^*_{crit}$ the near-singularity triggers a hybrid integration scheme, named sinh$^+$ in this work, details of which are provided in the following section. Here the adaptive integration and sinh transformation methods are combined; the sinh transformation is used in the region very close to the source point, and the adaptive scheme used in the more distant parts of the element. When the projection point lies outside the element ($\mathbf{x}^{p'} \notin \Gamma_e$, illustrated in Fig. 11), the extended sinh transformation in Section 4 is used.

5.1. Hybrid sinh$^+$ scheme

It has been shown that there is a truncation error term E_{trun} in Eqs. (26) and (33) due to the use of NURBS shape functions to replace the conventional Lagrange polynomials. In this section, we will discuss the influence of this term on the results and develop the new sinh$^+$ transformation method. As in the previous section, an arc describing a quarter of a circle will be studied, described by a quadratic NURBS with $\Xi = \{0, 0, 0, 1, 1, 1\}$, control points $P_1 = (3.0005, 0)$, $P_2 = (3.0005, 3.0005)$, $P_3 = (0, 3.0005)$ and weights $[1, \sqrt{2}/2, 1]$. We take the minimum distance to be $d = 5 \times 10^{-4}$ m.

From Eq. (33), we can obtain

$$E_{\text{trun}} = \left| r^2_{\text{exact}} - \left(d^2 + (\xi - \xi_p)^2 g_n(\xi) \right) \right| \tag{49}$$

where $r^2_{\text{exact}} = (x_1 - y_1)^2 + (x_2 - y_2)^2$ is the real square distance between the source point and field (Gauss) point. This square distance can be computed accurately since the coordinates of both points are known. Therefore, the following relative error can be used to describe the accuracy of the Taylor expansion in predicting the square distance r^2:

$$\text{Relative error} = \left| \frac{E_{\text{trun}}}{r^2_{\text{exact}}} \right| \tag{50}$$

Figs. 14(a) and 14(b) show the relative error comparisons when the projection point is located at the middle ($\xi_p = 0.5$) and end ($\xi_p = 1$) of the element, respectively. From the two figures we can see the growth of the truncation error with increasing distance between the field point and the projection point. The order referred to in these figures relates to the number of terms used in the Taylor series approximation. In Fig. 14(a), the reason for the fluctuation of the curves for order $= 3, 5$ is that the sign of the error changes at these points.

This behaviour leads us to propose the sinh$^+$ method as shown graphically in Fig. 15. In the computation of nearly singular integrals for an IGABEM boundary element with knot span $[\xi_1, \xi_2]$, we first compute the truncation error E_{trun} at each Gauss point. If E_{trun} exceeds a predefined tolerance eps at the points $\xi = \xi'_1$ and $\xi = \xi'_2$, the element will be subdivided into three parts $[\xi_1, \xi'_1]$, $[\xi'_1, \xi'_2]$ and $[\xi'_2, \xi_2]$ and the integral evaluated piecewise as

$$\int_{\xi_1}^{\xi_2} f(\xi) d\xi = \int_{\xi_1}^{\xi'_1} f(\xi) d\xi + \int_{\xi'_1}^{\xi'_2} f(\xi) d\xi + \int_{\xi'_2}^{\xi_2} f(\xi) d\xi \tag{51}$$

In the central sub-region $[\xi'_1, \xi'_2]$, since $E_{\text{trun}} < eps$, the sinh transformation method may be safely adopted and the scheme can benefit from its computational efficiency. The adaptive integral method will be used to compute the integrals on the subdivisions $[\xi_1, \xi'_1]$ and $[\xi'_2, \xi_2]$ since $E_{\text{trun}} > eps$. Note that the adaptive scheme will be efficient here since the interval of integration is not too close to the source point.

To show the effect of eps on the time taken to compute the integral and the accuracy, a single integral case (strong nearly singular integral with arc geometry in this section) is given in Figs. 16(a) and 16(b). It is noted that with the decreasing of eps the accuracy of the sinh$^+$ scheme will be significantly improved, with mild changes in CPU time.

5.2. Summary of overall integration strategy

The new scheme is summarised as follows. For all non-singular cases:

- if $d^* > d^*_{crit}$, the adaptive scheme is used.
- if $d^* < d^*_{crit}$, the sinh transformation is used for the portion of the element (closer to the source point) over which $E_{trun} \leq eps$, and the adaptive scheme is used for the more distant portions of the element as shown in Fig. 15.

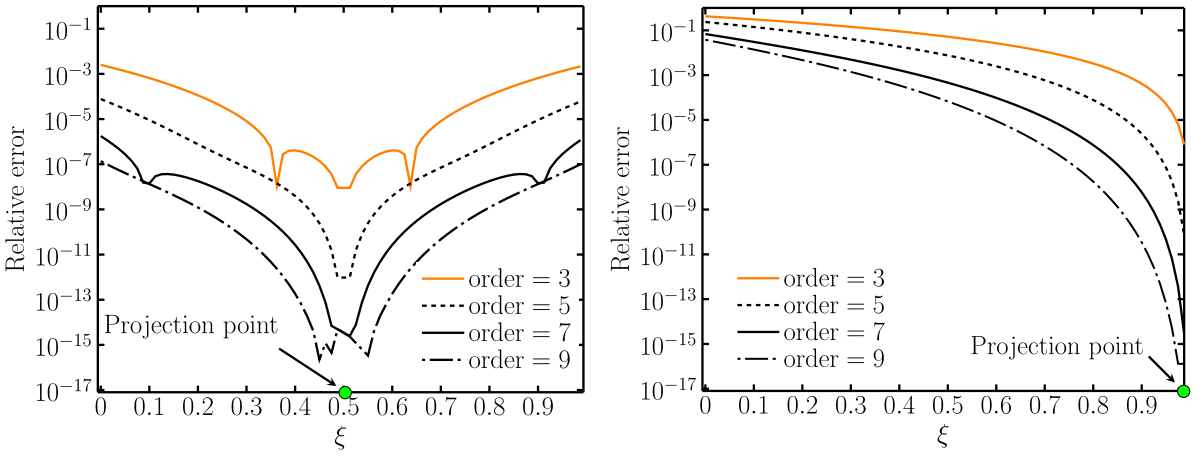

(a) $\mathbf{x}^p$ located at the middle of element

(b) $\mathbf{x}^p$ located at the end of element

Fig. 14. Comparisons of relative errors for different orders of Taylor expansion.

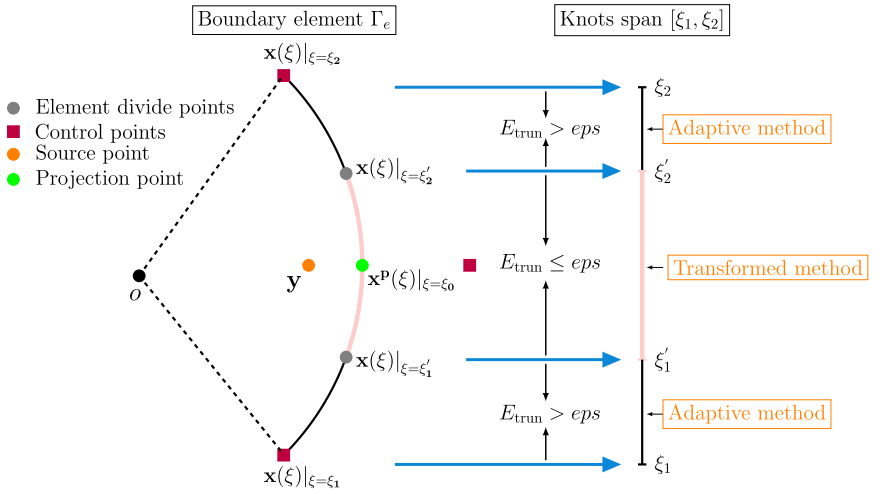

Fig. 15. Choice of integral method based on the truncation errors E_{trun} of Taylor expansion.

- if the projection point lies outside the element, then the extended sinh transformation is used to replace the conventional sinh transformation
- in some cases, $E_{trun} \leq eps$ over the entire element, in which case the adaptive scheme is not used

6. Numerical examples

In this section, through several numerical examples, the accuracy and effectiveness of the IGABEM using the sinh$^+$ scheme for coating structures are demonstrated. The examples involve a substrate with a coating, and material properties are typical of the materials used in a superalloy turbine blade with a thermal barrier coating. All material properties are taken from Padture et al. [34]. All analyses are steady state heat transfer, and in this section we use the notation T (playing the role of u in the earlier sections of this paper) to emphasise that this is a temperature. All examples are run in 2D, though we make use of surface plots as a revealing way to display some relative errors. To carry out the accuracy and convergence analysis, two types of errors are considered: a relative error defined in Eq. (44)

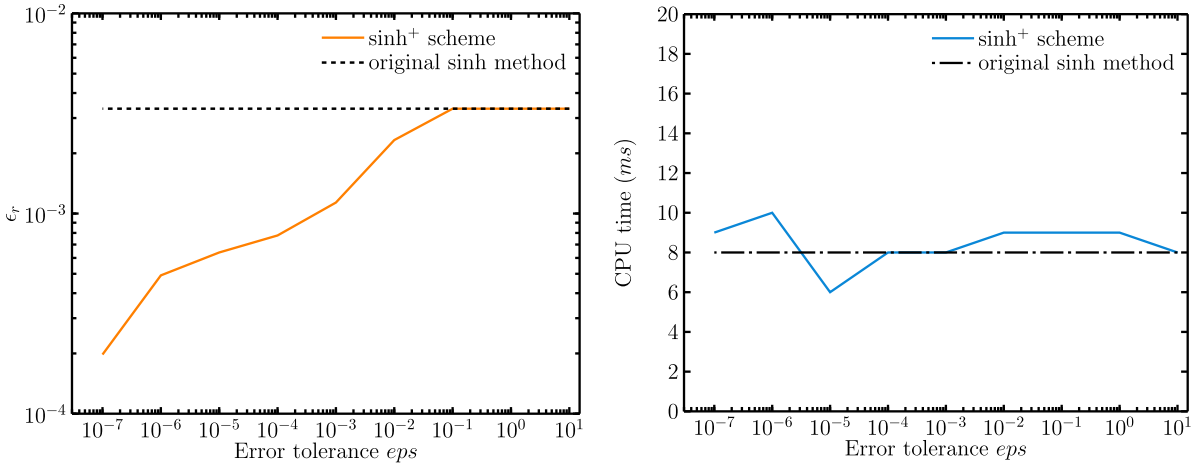

(a) Accuracy of results with various *eps*

(b) CPU time of computation with various *eps*

Fig. 16. The impact of various *eps* on the accuracy and CPU time of the nearly singular integration.

and L_2 relative error norm with respect to a reference solution T_{ref} defined by

$$E_2(T_{\text{num}};\, \Gamma) = \frac{\|T_{\text{num}} - T_{\text{ref}}\|_{L_2(\Gamma)}}{\|T_{\text{ref}}\|_{L_2(\Gamma)}} \tag{52}$$

where Γ is the boundary, portion of the boundary, or other contour over which the norm is taken, T_{num} is the temperature as predicted by the present numerical scheme, and the L_2 norm is

$$\|f\|_{L_2(\Gamma)} = \sqrt{\int_\Gamma f^2 d\Gamma}$$

Unless otherwise stated, we take the tolerance $eps = 10^{-6}$ in the sinh$^+$ scheme for all examples. For examples 6.2–6.4, the original parametric definition of the substrate and coating geometry is given by knot vector $\Xi = \{0, 0, 0, 1, 1, 2, 2, 3, 3, 4, 4, 4\}$. The degree of the NURBS basis functions is $p = 2$. Unit weights are used for a square boundary and weights $w = [1, \frac{\sqrt{2}}{2}, 1, \frac{\sqrt{2}}{2}, 1, \frac{\sqrt{2}}{2}, 1, \frac{\sqrt{2}}{2}, 1]$ are adopted for a circular boundary.

6.1. Heat transfer through plane wall with multilayer coating structures

In practice we often encounter plane walls that consist of several layers of different materials. Consider a 1×2 m rectangular plate, as shown in Fig. 17 with thermal conductivity 22 W/m · K. Both sides are covered by a ceramic coating structure made of Y_2O_3-stabilised ZrO_2 (YSZ) with thermal conductivity 2.3 W/m · K which provides the thermal insulation so that the one-dimensional problem will have a temperature distribution as plotted in the figure with T_1, T_2, T_3, T_4 being temperatures at the key locations. In the computation, the thickness δ of the coating structure varies from 0.5 to 10^{-8} m. The temperatures on both sides are prescribed as $T_1 = 150$ °C and $T_4 = 10$ °C. All upper and lower boundaries are insulated, i.e. $\nabla T \cdot \mathbf{n} = 0$. We define boundaries $\Gamma_{\bar{q}}$ as the union of the (horizontal) insulated boundaries, and $\Gamma_{\texttt{int}}$ as the union of the two interfaces. The initial parametric definition of the substrate and coating geometry is given by two knot vectors $\Xi_1 = \{0, 0, 0, 1, 1, 2, 2, 3, 3, 4, 4, 5, 5, 6, 6, 6\}$ and $\Xi_2 = \{0, 0, 0, 1, 1, 2, 2, 3, 3, 4, 4, 4\}$, respectively. The NURBS basis functions with polynomial degree $p = 2$ and unit weights are used.

In Fig. 18(a) we present the L_2 relative error norm $E_2(T_{\text{num}}; \Gamma_{\bar{q}} \cup \Gamma_{\texttt{int}})$ when different integration schemes and different coating thickness δ are considered. It is evident that when $\delta > 0.1$ m, all methods can obtain accurate results. However, with the reduction of thickness δ the results obtained by the regular Gauss quadrature become unsatisfactory. In contrast, the sinh$^+$ and adaptive schemes can obtain accurate results for coating thickness δ as small as 10^{-8} m. In Fig. 18(b), the CPU time of the different analysis methods is given with the reduction of coating

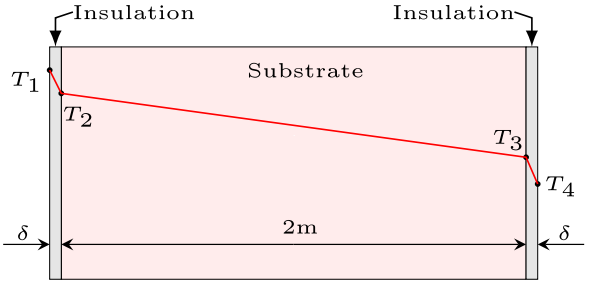

Fig. 17. Heat transfer through a model with double flat coatings.

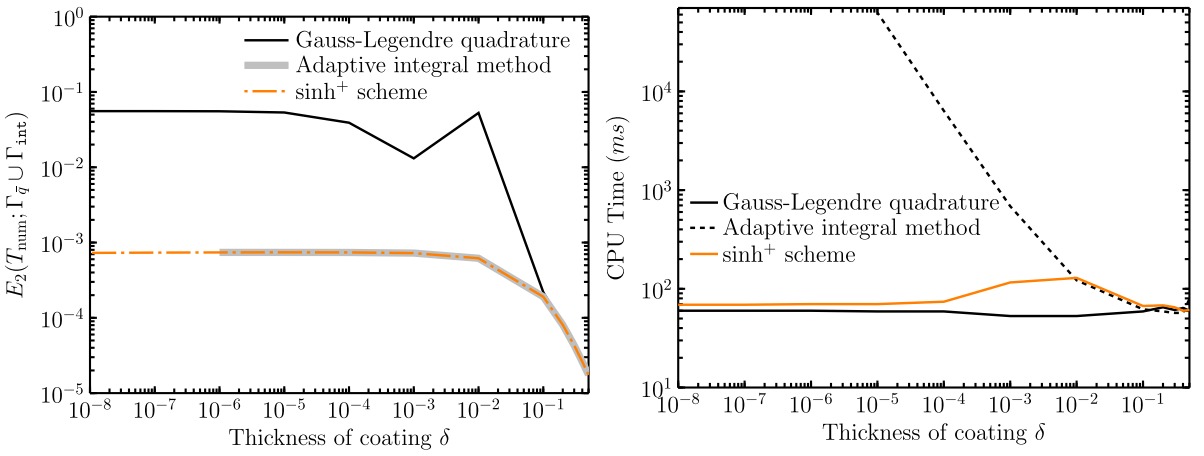

(a) L_2 relative error norm $E_2(T_{\text{num}}; \Gamma_{\bar{q}} \cup \Gamma_{\text{int}})$

(b) Comparison of CPU time for different methods

Fig. 18. Comparisons of accuracy and efficiency.

thickness δ. When $\delta > 10^{-2}$ m the sinh$^+$ scheme will use a little more time than the adaptive method due to the overhead in selecting the appropriate integration scheme. However, for $\delta \leq 10^{-2}$ m, the CPU time of the adaptive scheme increases dramatically, while the CPU time of the sinh$^+$ scheme remains fixed at around 10^2 ms.

To further illustrate the effective of the sinh$^+$ scheme, the numerical temperature distribution and its relative error inside the substrate when $\delta = 10^{-5}$ m are given in Figs. 19(a) and 19(b), respectively.

6.2. *Heat transfer through cylinder with multilayer coating structures*

In the second example we study the heat transfer through a cylinder with multilayer coatings as shown in Fig. 20. The conductivity of the superalloy substrate is taken as 22 W/m · K and the inner and outer diameters of the substrate are $r_1, r_2 = 2, 3$ m. As shown in the figure, both sides of the substrate are covered with a YSZ coating of thickness δ m and having thermal conductivity 2.3 W/m · K. In the computation, the coating thickness δ varies from 0.5 to 10^{-7} m. The temperatures on the inner and outer diameters are prescribed as boundary conditions, being $T_1 = 80$ °C and $T_4 = 200$ °C.

In Fig. 21 we present the L_2 relative error norm $E_2(T_{\text{num}}; \Gamma_{\text{int}})$ where Γ_{int} is the union of the interfaces between the substrate and its coatings; results for different integration schemes and for different values of δ are shown. From this figure, some similar conclusions as for Section 6.1 can be drawn. Firstly, all the methods are effective when $\delta > 0.1$ m but the results obtained by the regular Gauss quadrature become unsatisfactory for smaller δ. Again, the sinh$^+$ and adaptive schemes can still deliver accurate results for thickness δ as small as 10^{-7} m. The CPU time associated with the different methods is given in Fig. 22. Similar conclusions can be drawn as in the previous example with the CPU time of the sinh$^+$ scheme stabilising at around 10^3 ms for small δ.

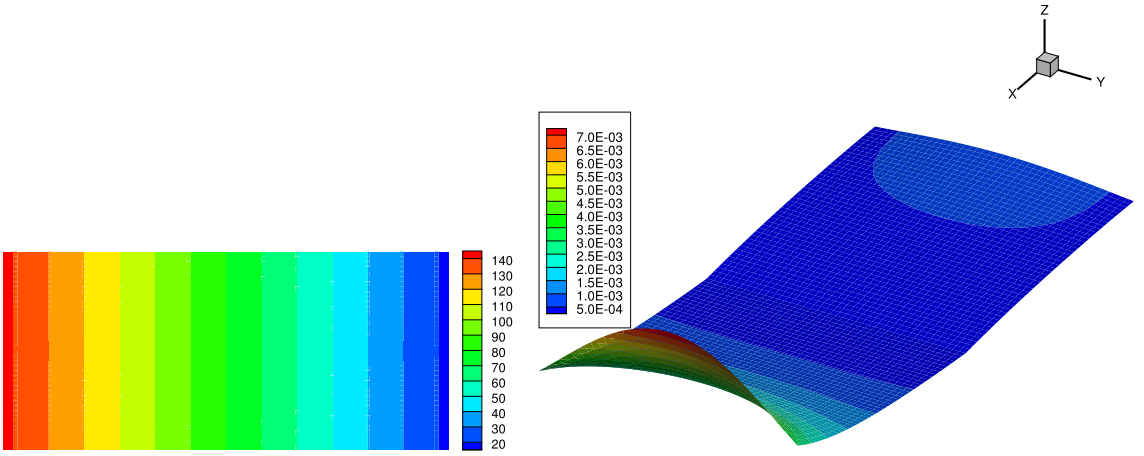

(a) Temperature distribution inside the matrix

(b) Relative error of the computed points

Fig. 19. Temperature distribution and relative error inside the matrix.

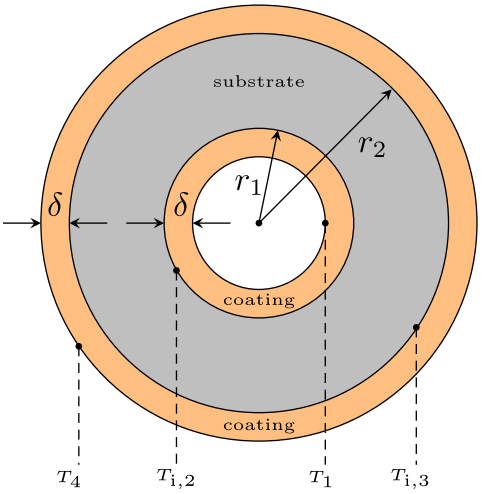

Fig. 20. The thermal resistance network for heat transfer through a cylinder with multilayer coating structures.

Fig. 23 shows the convergence of the L_2 relative error norm $E_2(T_{\text{num}}; \Gamma_{\text{int}})$ as the number of degrees of freedom (ndof) increases from 48 to 480 with different coating thickness δ. The convergence can be clearly seen even when the thickness of the ceramic coating is as small as 1 μm (10^{-6} m). The reason for the increase in relative error norm for small $\delta \leq 10^{-3}$ m is that in the sinh$^+$ scheme the sinh transformation is now activated, as $d^* < d^*_{\text{crit}}$, to improve the efficiency. We are able to tolerate this additional error because *the integration scheme has been tuned to deliver acceptable engineering accuracy at the optimal computational cost*.

Fig. 24 shows the behaviour of the L_2 relative error norm $E_2(T_{\text{num}}; \Gamma_{\text{int}})$ with the coating thickness δ. As δ reduces from 0.5 to 10^{-3} m the error gradually increases. For $\delta < 10^{-3}$ m the sinh$^+$ scheme activates the sinh transformation in evaluating the nearly singular integrals; in this range, the L_2 relative error norm remains stable, stabilising at smaller errors as the model size increases.

As shown in Fig. 15, the choice of the appropriate integration method in the proposed sinh$^+$ scheme depends on the values of error tolerance *eps* and the truncation error E_{trun} of the Taylor expansion. In Fig. 25 we study the effect of *eps* and ndof on the L_2 relative error norm $E_2(T_{\text{num}}; \Gamma_{\text{int}})$ when 9 Taylor series terms are used. The influence of the

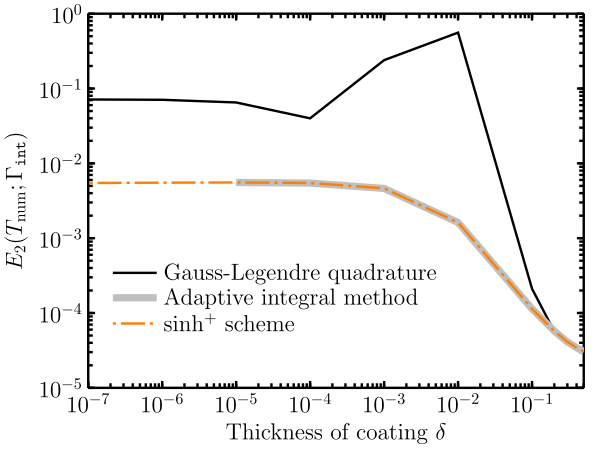

Fig. 21. L_2 relative error norm $E_2(T_{\text{num}}; \Gamma_{\texttt{int}})$.

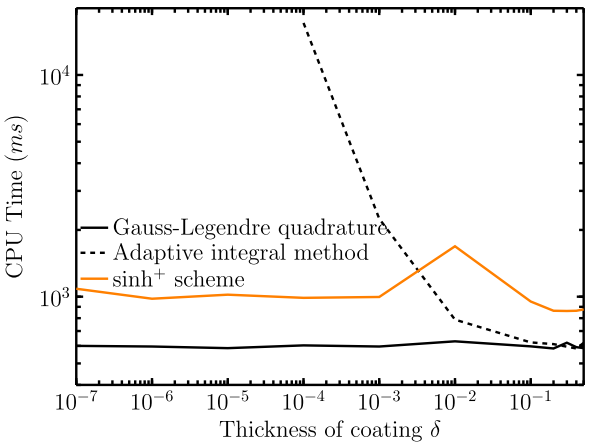

Fig. 22. Comparisons of CPU time for different methods.

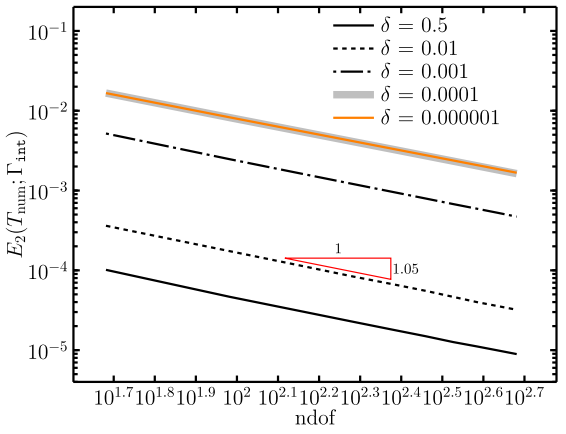

Fig. 23. Convergence of L_2 relative error norm $E_2(T_{\text{num}}; \Gamma_{\texttt{int}})$ with ndof.

tolerance *eps* can be clearly seen for the coarser discretisations when ndof $= 48$, with the L_2 norm error stabilising as *eps* reduces. When the mesh is refined, the aspect ratio d^* will increase to the extent that the sinh$^+$ scheme uses

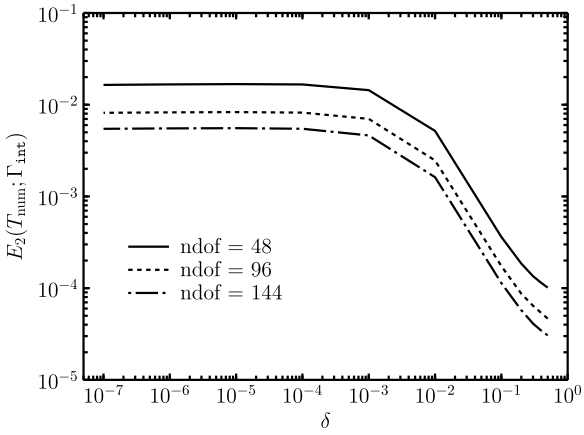

Fig. 24. L_2 relative error norm $E_2(T_{\text{num}}; \Gamma_{\text{int}})$ vs. δ.

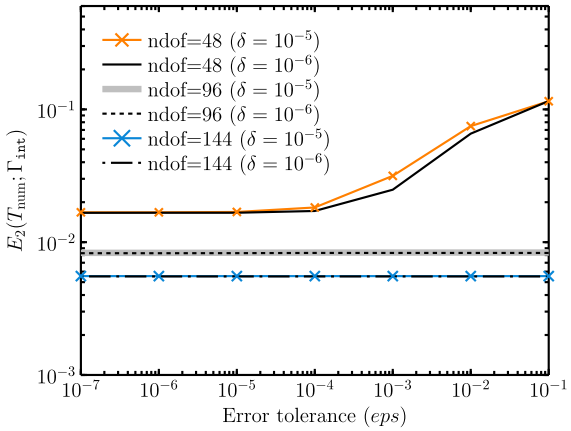

Fig. 25. L_2 relative error norm $E_2(T_{\text{num}}; \Gamma_{\text{int}})$ when different error tolerances are used in sinh$^+$(illustrated in Fig. 15).

only the adaptive scheme. In this range, the solution accuracy is independent of tolerance eps. It should be noted that when $eps \gg 10^{-1}$, the sinh$^+$ scheme will degenerate to the original sinh method.

Figs. 26(a) and 26(b) show the temperature contours and the relative error through the cylinder for the case $\delta = 10^{-6}$ m.

6.3. Convective heat transfer through hollow cylinder with coating structure

Convection problems are particularly important in heat transfer applications such as those found in turbomachinery. For a turbine blade, it is very difficult to obtain the boundary temperature, while the ambient fluid temperature adjacent to the material surface can usually be obtained more readily. In this example we make some modifications to the example in Section 6.2 to explore different numerical features of the different schemes and better simulate a working turbomachinery environment. For simplicity we remove the coating on the outer diameter, we will explore the effect of different coating materials (having different thermal conductivity), and we apply on the inner diameter of the remaining coating a convection boundary condition given by

$$k\frac{\partial T}{\partial n} = -h(T_f - T) \tag{53}$$

where T_f is the temperature of the fluid and h is the heat transfer coefficient.

As is shown in Fig. 27(a), we model a superalloy cylinder substrate with inner diameter of 2 m and outer diameter of 3 m. The inner surface of the substrate is covered by a ceramic coating of thickness δ and thermal conductivity

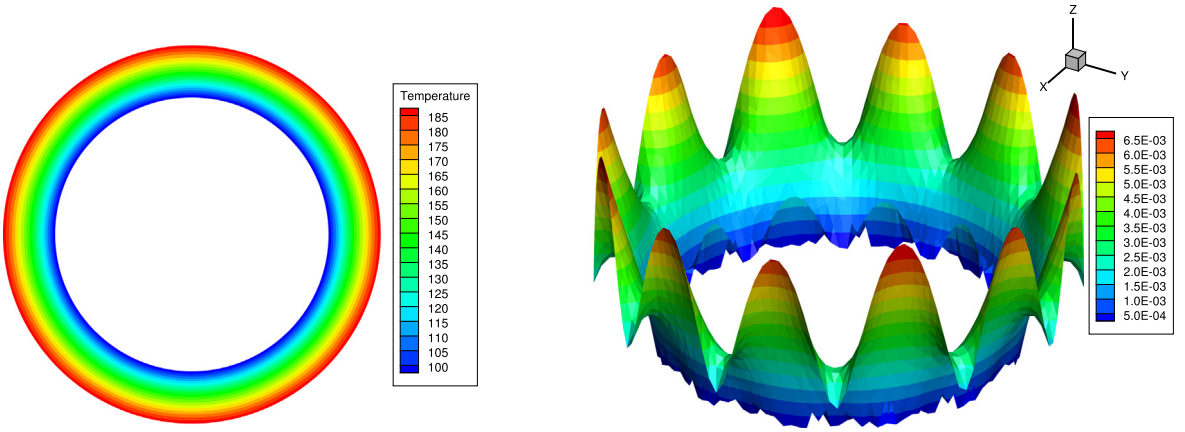

(a) Results computed by $\sinh^+$ scheme

(b) Relative error of the computed points

Fig. 26. Temperature distribution inside the substrate and its relative errors when $\delta = 10^{-6}$.

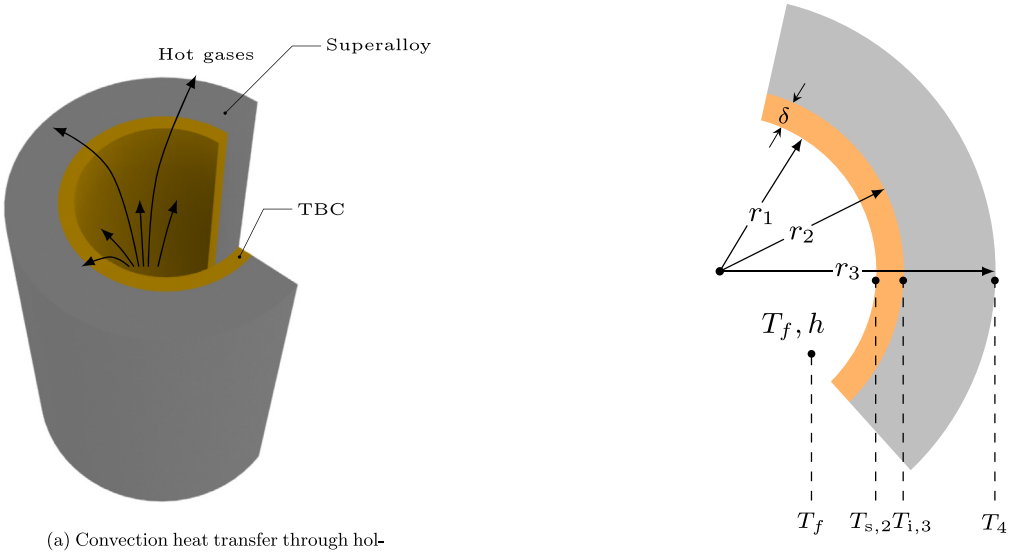

(a) Convection heat transfer through hollow cylinder with coating structure

(b) Cross section of heat transfer model with convective surface condition

Fig. 27. Convection heat transfer model.

2.3 W/m · K. The hollow superalloy cylinder substrate has a thermal conductivity of 22 W/m · K and its outer surface maintains a constant temperature of $T_4 = 800$ °C. The thermal barrier coating is exposed to hot gases at temperature $T_f = 1700$ °C and a heat transfer coefficient $h = 1000$ W/m^2 · K applies [34,86]. In the computation, the coating thickness δ varies from 0.5 to 10^{-7} m. Note that Fig. 27(a) is included for diagrammatic purposes, and the analysis is performed for the full 360° cylinder in 2D.

Fig. 28 shows the L_2 relative error norm of the interface temperatures, $E_2(T_{\text{num}}; \Gamma_{\text{int}})$, for coating thicknesses down to 10^{-7} m. Once again, we see the $\sinh^+$ scheme outperforms Gauss–Legendre quadrature and is able to deliver accurate results from small models, in this case as few as ndof = 32, and is stable at very small coating thicknesses. A significant improvement in accuracy can be seen when the model is refined. To further illustrate the accuracy of the

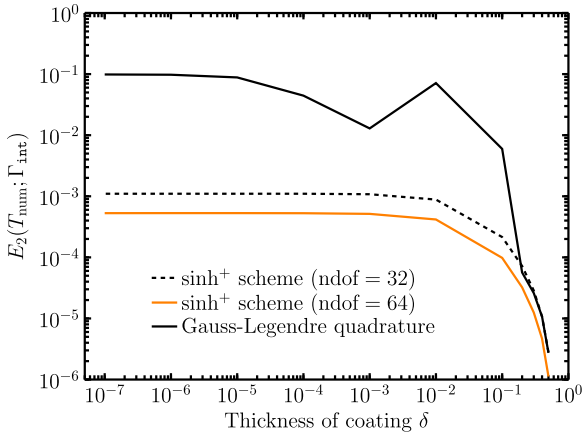

Fig. 28. L_2 norm $E_2(T_{\text{num}}; \Gamma_{\text{int}})$.

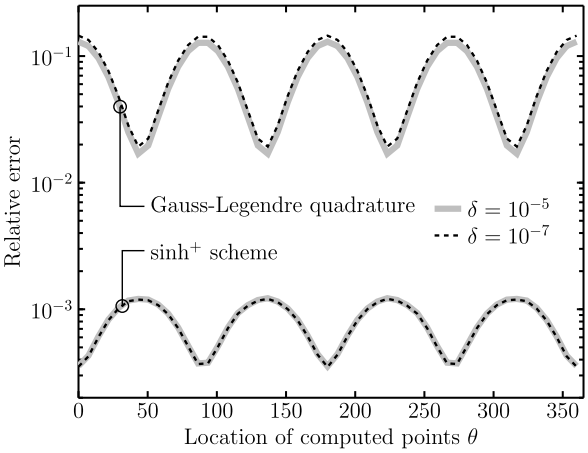

Fig. 29. Relative errors along S_1 with $\delta = 10^{-5}$ and 10^{-7}.

method to solve convective heat transfer models with a coating, we plot in Fig. 29 the relative error in the temperature at points inside the substrate lying on the contour S_1, which is defined by

$$S_1 = \{(x, y); x = r_0 \cos\theta, y = r_0 \sin\theta, \theta \in [0, 2\pi), r_0 = 2.5 \text{ m}\} \tag{54}$$

The relative error obtained by the sinh$^+$ scheme is considerably smaller than that of the regular Gauss quadrature, as expected, though it retains an oscillatory nature. This can be attributed to the coarse discretisation; although the geometry is exact with our IGABEM model, there is a periodicity in the control point locations that is reflected in the solution. However, the relative error remains stable as δ changes from 10^{-5} to 10^{-7} m.

Fig. 30 studies the convergence of the IGABEM scheme using sinh$^+$ when we refine the mesh for different coating thicknesses. For a fixed thickness δ the convergence of the method is demonstrated well with increasing model refinement. Otherwise, we draw the same conclusions as from Fig. 23, in that the sinh$^+$ scheme is performing well in delivering results of good engineering accuracy for small δ, at which the algorithm activates the sinh transformation in addition to the adaptive scheme.

Fig. 31 shows the temperature difference across the coating. We consider coatings made of four commonly used coating materials: $BaLa_2Ti_3O_{10}$ ($k = 0.7$ W/m $\cdot$ K) [87], $La_2Zr_2O_7$ ($k = 1.56$ W/m $\cdot$ K) [88], YSZ ($k = 2.3$ W/m $\cdot$ K) [34] and $BaZrO_3$ ($k = 3.42$ W/m $\cdot$ K) [89]. The graphs show the reduction in the insulation capacity of the coating as its thickness δ reduces. We can also verify numerically that the greater the conductivity

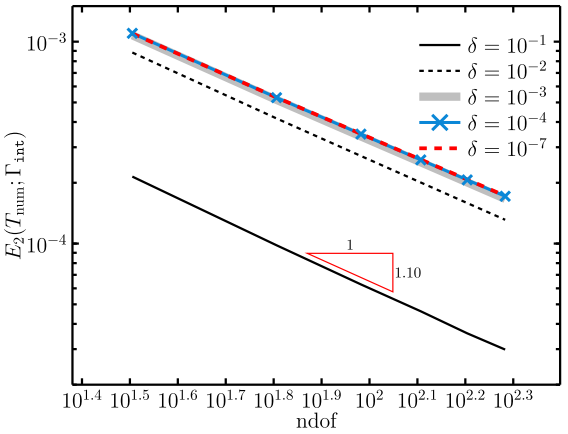

Fig. 30. Solution convergence for different δ.

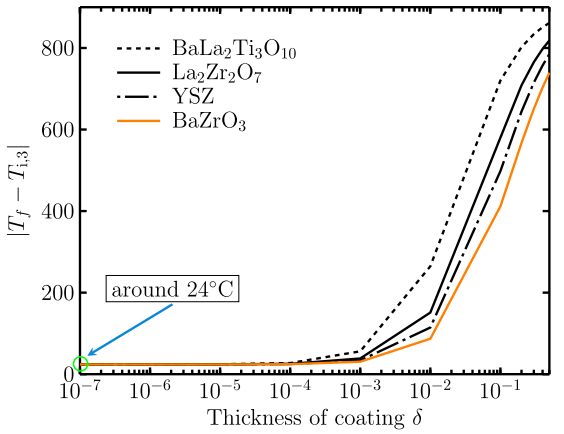

Fig. 31. Temperature drop across the coating.

of the coating, the smaller will be its heat insulation capacity. However, as the coating thickness becomes small, reducing to 10^{-7} m, the relationship between its heat insulation capacity and its thermal conductivity is not obvious, as the curves for all materials become coincident.

Finally, using the initial parameters, the temperature distribution inside the substrate and its relative error for coating thickness $\delta = 10^{-6}$ m are given in Figs. 32 and 33, respectively.

6.4. Convection heat transfer through a tube in a square cross-section

In our final example, shown in Fig. 34(a), hot steam is carried from a combined heat and power generation plant by a tube centred in a 6 m square cross-section solid material with thermal conductivity of 22 W/m · K. As shown in Figs. 34(a) and 34(b), the inner side of the substrate (at radius $r = 2$ m) is covered by ceramic (YSZ) coating of thickness δ and thermal conductivity 2.3 W/m · K. In Fig. 34(b), the left and right surface temperatures on the left and right edges of the substrate are prescribed constant at $T_4 = 500$ °C and $T_5 = 100$ °C, respectively. The coating inside the substrate is exposed internally to hot gases at a temperature $T_f = 1700$ °C, and a heat transfer coefficient of 1000 W/m^2·K applies. Again, the 3D view in Fig. 34(a) is for diagrammatic purposes only; all analyses are performed in 2D.

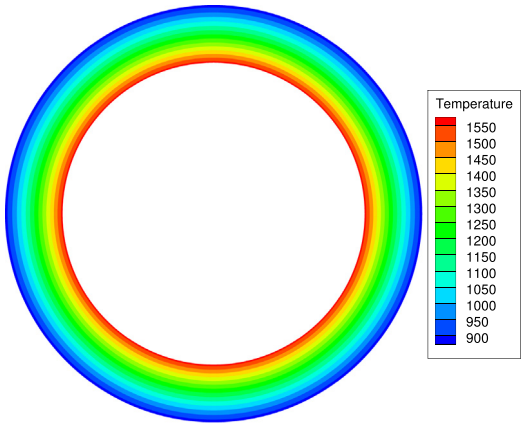

Fig. 32. Temperature distribution with $\delta = 10^{-6}$ m.

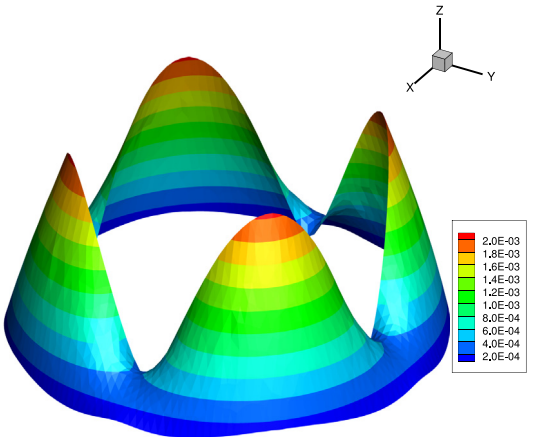

Fig. 33. Relative error in the temperature.

For this problem, an analytical solution is not available, and the convergence of the problem is established by taking a very refined BEM model as the reference solution. Thus we define an error metric

$$\text{Error} = \frac{1}{N}\sum_{n=1}^{N}\left|\frac{T_n^i - T_n^{32}}{T_n^{32}}\right| \tag{55}$$

where N is the number of evaluation points used to compute the error, and T_n^i is the temperature at the nth evaluation point in the IGABEM model at refinement level i. The refinement between levels is accomplished by uniform knot insertion. It can be seen from the equation that the solution at refinement level 32 (ndof $= 1024$) is used as the reference solution.

As our evaluation points we take 50 uniformly spaced points along the contour S_1, defined in (54). Fig. 35 shows the solution convergence in the metric (55) when the NURBS is refined. We consider a coating of thickness $\delta = 10^{-6}$ m. The table in the figure gives the corresponding model size in ndof at each refinement level. Here, the impact of various *eps* on the overall accuracy follows the same pattern as shown in Fig. 25 for the previous example.

Fig. 36 shows the temperature $T_{i,3}$ at the interface between the substrate and the coating for different coating thicknesses δ. Again we see the improved thermal insulation with thicker coatings, but also we see the increased variation in the temperature around the circumference of the interface. Finally, Figs. 37(a) and 37(b) show the temperature distribution inside the substrate for coating thicknesses $\delta = 10^{-1}$ and 10^{-6} m, respectively.

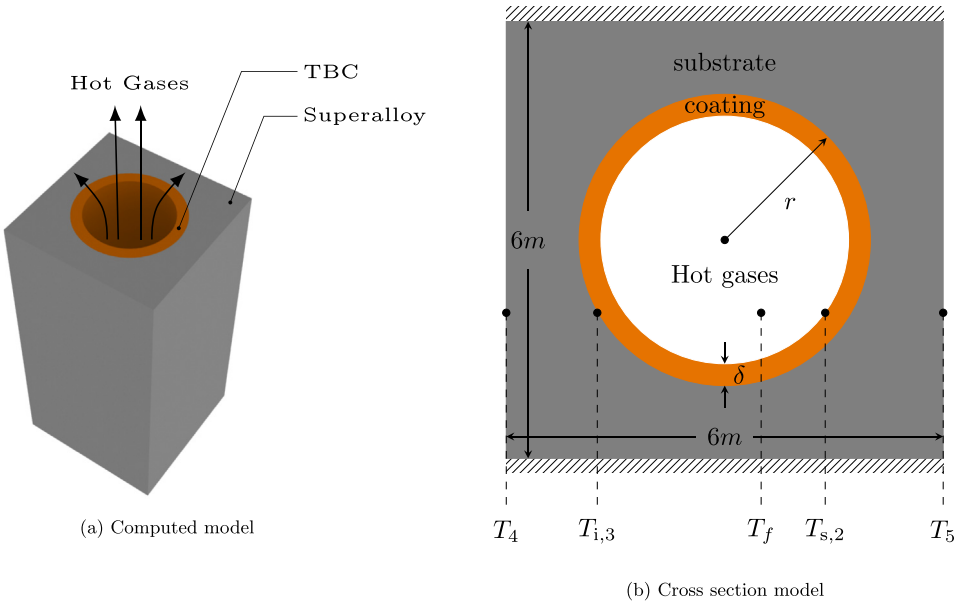

(a) Computed model

(b) Cross section model

Fig. 34. Convection heat transfer model.

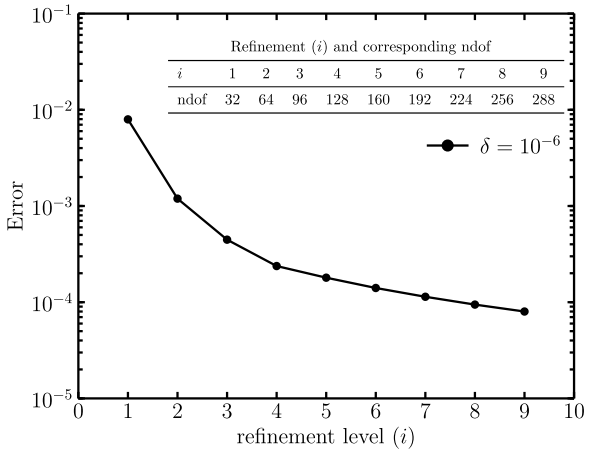

Fig. 35. Solution convergence.

7. Conclusion

In this paper, engineering systems with thermal barrier coatings are studied using the isogeometric boundary element method (IGABEM). An essential feature of these problems is the small thickness of the coating structures, typically 1 to 5 μm [34], and it is demonstrated that a naive IGABEM implementation using a standard quadrature scheme, that does not specifically deal with this special geometry, is unable to deliver results of acceptable engineering accuracy.

An analysis is carried out on the errors and computational efficiency of available methods for evaluating nearly singular integrals in the BEM. We adapt these methods to the IGABEM and show that using only one of the examined methods does not yield a satisfactory balance between accuracy and efficiency. We develop and propose the new $\sinh^+$ scheme that combines the benefits of the sinh transformation (of, amongst others, Gu et al. [69]) and adaptive integration scheme (of Gao et al. [54]). In order to make the scheme robust, we further extend the sinh transformation by using the analytical extension of the NURBS curve to accommodate cases in which the projection of the source point lies outside the physical domain of the element.

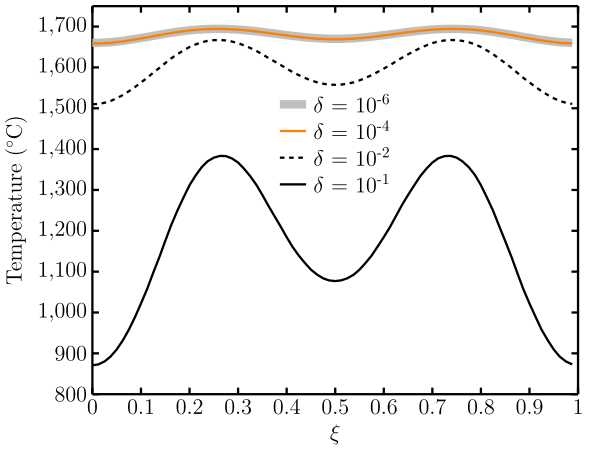

Fig. 36. Interface temperature distributions.

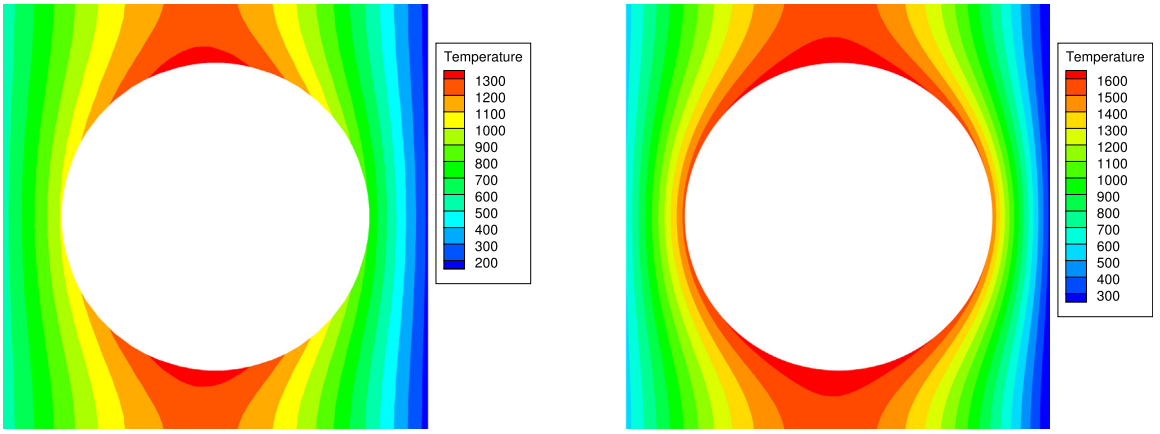

(a) $\delta = 0.1$ m (b) $\delta = 10^{-6}$ m

Fig. 37. Temperature distribution in the substrate for the cases $\delta = 0.1$ and 10^{-6} m.

The resulting sinh$^+$ scheme thereby maintains the computation accuracy across the full range of coating thicknesses by controlling the truncation error in the Taylor expansion of the BEM square distance function for NURBS discretisations. An important feature of the work is that the integration scheme is tuned to deliver results of engineering accuracy in the optimal computation time. The scheme is adaptable, by changing the tolerance *eps*, to enable engineers to achieve a different balance between accuracy and computational efficiency as may be required for different applications.

A range of numerical examples together demonstrate that the new sinh$^+$ scheme delivers highly accurate solutions in a computationally efficient manner in the solution of engineering problems with thermal barrier coatings.

Acknowledgements

The research is supported by the National Natural Science Foundation of China (11672038, 11272054). The authors also acknowledge financial supports from the Graduate Technological Innovation Project of Beijing Institute of Technology, China (2017CX10033) and the China Scholarship Council.

References

[1] T.J.R. Hughes, J.A. Cottrell, Y. Bazilevs, Isogeometric analysis: CAD, finite elements, NURBS, exact geometry and mesh refinement, Comput. Methods Appl. Mech. Engrg. 194 (39–41) (2005) 4135–4195.

[2] D. Schillinger, L. Dede, M.A. Scott, J.A. Evans, M.J. Borden, E. Rank, T.J.R. Hughes, An isogeometric design-through-analysis methodology based on adaptive hierarchical refinement of NURBS, immersed boundary methods, and T-spline CAD surfaces, Comput. Methods Appl. Mech. Engrg. 249 (2012) 116–150.

[3] Y. Bazilevs, V.M. Calo, T.J.R. Hughes, Y. Zhang, Isogeometric fluid-structure interaction: theory, algorithms, and computations, Comput. Mech. 43 (1) (2008) 3–37.

[4] Y. Bazilevs, M.-C. Hsu, M.A. Scott, Isogeometric fluid–structure interaction analysis with emphasis on non-matching discretizations, and with application to wind turbines, Comput. Methods Appl. Mech. Engrg. 249 (2012) 28–41.

[5] A. Buffa, G. Sangalli, R. Vázquez, Isogeometric analysis in electromagnetics: B-splines approximation, Comput. Methods Appl. Mech. Engrg. 199 (17–20) (2010) 1143–1152.

[6] J.A. Cottrell, A. Reali, Y. Bazilevs, T.J.R. Hughes, Isogeometric analysis of structural vibrations, Comput. Methods Appl. Mech. Engrg. 195 (41–43) (2006) 5257–5296.

[7] Y. Bazilevs, V.M. Calo, J.A. Cottrell, J.A. Evans, T.J.R. Hughes, S. Lipton, M.A. Scott, T.W. Sederberg, Isogeometric analysis using T-splines, Comput. Methods Appl. Mech. Engrg. 199 (5–8) (2010) 229–263.

[8] N. Nguyen-Thanh, J. Kiendl, H. Nguyen-Xuan, R. Wüchner, K.-U. Bletzinger, Y. Bazilevs, T. Rabczuk, Rotation free isogeometric thin shell analysis using PHT-splines, Comput. Methods Appl. Mech. Engrg. 200 (47–48) (2011) 3410–3424.

[9] N. Nguyen-Thanh, H. Nguyen-Xuan, S.P.A. Bordas, T. Rabczuk, Isogeometric analysis using polynomial splines over hierarchical T-meshes for two-dimensional elastic solids, Comput. Methods Appl. Mech. Engrg. 200 (21–22) (2011) 1892–1908.

[10] P. Wang, J. Xu, J. Deng, F. Chen, Adaptive isogeometric analysis using rational PHT-splines, Comput. Aided Des. 43 (11) (2011) 1438–1448.

[11] B. Marussig, J. Zechner, G. Beer, T.-P. Fries, Stable isogeometric analysis of trimmed geometries, Comput. Methods Appl. Mech. Engrg. 316 (2017) 497–521.

[12] D.N. Arnold, L. Li, Finite element exterior calculus with lower-order terms, Math. Comp. (2016).

[13] D.N. Arnold, J. Saranen, On the asymptotic convergence of spline collocation methods for partial differential equations, SIAM J. Numer. Anal. 21 (3) (1984) 459–472.

[14] J.A. Ligget, J.R. Salmon, Cubic spline boundary elements, Internat. J. Numer. Methods Engrg. 17 (4) (1981) 543–556.

[15] J.J.S.P. Cabral, L.C. Wrobel, C.A. Brebbia, A BEM formulation using B-splines: I-uniform blending functions, Eng. Anal. Bound. Elem. 7 (3) (1990) 136–144.

[16] M. Yu, E. Kuffel, Spline element for boundary element method, IEEE Trans. Magn. 30 (5) (1994) 2905–2907.

[17] E. Turco, M. Aristodemo, A three-dimensional B-spline boundary element, Comput. Methods Appl. Mech. Engrg. 155 (1) (1998) 119–128.

[18] F. Rivas, L. Valle, M.F. Cátedra, A moment method formulation for the analysis of wire antennas attached to arbitrary conducting bodies defined by parametric surfaces, Appl. Comput. Electromagn. Soc. J. 11 (1996) 32–39.

[19] R.N. Simpson, S.P.A. Bordas, J. Trevelyan, T. Rabczuk, A two-dimensional isogeometric boundary element method for elastostatic analysis, Comput. Methods Appl. Mech. Engrg. 209 (2012) 87–100.

[20] R.N. Simpson, S.P.A. Bordas, H. Lian, J. Trevelyan, An isogeometric boundary element method for elastostatic analysis: 2D implementation aspects, Comput. Struct. 118 (2013) 2–12.

[21] M.A. Scott, R.N. Simpson, J.A. Evans, S. Lipton, S.P.A. Bordas, T.J.R. Hughes, T.W. Sederberg, Isogeometric boundary element analysis using unstructured T-splines, Comput. Methods Appl. Mech. Engrg. 254 (2013) 197–221.

[22] Y.J. Wang, D.J. Benson, Multi-patch nonsingular isogeometric boundary element analysis in 3D, Comput. Methods Appl. Mech. Engrg. 293 (2015) 71–91.

[23] K. Li, X. Qian, Isogeometric analysis and shape optimization via boundary integral, Comput. Aided Des. 43 (11) (2011) 1427–1437.

[24] H. Lian, P. Kerfriden, S.P.A. Bordas, Implementation of regularized isogeometric boundary element methods for gradient-based shape optimization in two-dimensional linear elasticity, Internat. J. Numer. Methods Engrg. 106 (12) (2016) 972–1017.

[25] M.J. Peake, J. Trevelyan, G. Coates, Extended isogeometric boundary element method (XIBEM) for two-dimensional Helmholtz problems, Comput. Methods Appl. Mech. Engrg. 259 (2013) 93–102.

[26] R.N. Simpson, M.A. Scott, M. Taus, D.C. Thomas, H. Lian, Acoustic isogeometric boundary element analysis, Comput. Methods Appl. Mech. Engrg. 269 (2014) 265–290.

[27] M.J. Peake, J. Trevelyan, G. Coates, Extended isogeometric boundary element method (XIBEM) for three-dimensional medium-wave acoustic scattering problems, Comput. Methods Appl. Mech. Engrg. 284 (2015) 762–780.

[28] R.N. Simpson, Z. Liu, Acceleration of isogeometric boundary element analysis through a black-box fast multipole method, Eng. Anal. Bound. Elem. 66 (2016) 168–182.

[29] R.N. Simpson, Z. Liu, R. Vazquez, J.A. Evans, An isogeometric boundary element method for electromagnetic scattering with compatible B-spline discretizations, J. Comput. Phys. 362 (2018) 264–289.

[30] X. Peng, E. Atroshchenko, P. Kerfriden, S.P.A. Bordas, Isogeometric boundary element methods for three dimensional static fracture and fatigue crack growth, Comput. Methods Appl. Mech. Engrg. 316 (2017) 151–185.

[31] B. Marussig, J. Zechner, G. Beer, T.-P. Fries, Fast isogeometric boundary element method based on independent field approximation, Comput. Methods Appl. Mech. Engrg. 284 (2015) 458–488.

[32] L.S. Campos, É.L. de Albuquerque, L.C. Wrobel, An ACA accelerated isogeometric boundary element analysis of potential problems with non-uniform boundary conditions, Eng. Anal. Bound. Elem. 80 (2017) 108–115.

[33] S. Li, J. Trevelyan, W. Zhang, D. Wang, Accelerating isogeometric boundary element analysis for 3-dimensional elastostatics problems through black-box fast multipole method with proper generalized decomposition, Internat. J. Numer. Methods Engrg. 114 (9) (2018) 975–998.
[34] N.P. Padture, M. Gell, E.H. Jordan, Thermal barrier coatings for gas-turbine engine applications, Science 296 (5566) (2002) 280–284.
[35] V. Sladek, J. Sladek, Singular Integrals in Boundary Element Methods (Advances in Boundary Elements), WIT Press, 1998.
[36] J.C.F. Telles, A self-adaptive co-ordinate transformation for efficient numerical evaluation of general boundary element integrals, Internat. J. Numer. Methods Engrg. 24 (5) (1987) 959–973.
[37] K. Hayami, A Projection Transformation Method for Nearly Singular Surface Boundary Element Integrals, Springer-Verlag Berlin Heidelberg, 1992.
[38] K. Hayami, H. Matsumoto, A numerical quadrature for nearly singular boundary element integrals, Eng. Anal. Bound. Elem. 13 (2) (1994) 143–154.
[39] V. Sladek, J. Sladek, M. Tanaka, Numerical integration of logarithmic and nearly logarithmic singularity in BEMs, Appl. Math. Model. 25 (11) (2001) 901–922.
[40] G.S. Padhi, R.A. Shenoi, S.S.J. Moy, M.A. McCarthy, Analytic integration of kernel shape function product integrals in the boundary element method, Comput. Struct. 79 (14) (2001) 1325–1333.
[41] Z. Niu, W.L. Wendland, X. Wang, H. Zhou, A semi-analytical algorithm for the evaluation of the nearly singular integrals in three-dimensional boundary element methods, Comput. Methods Appl. Mech. Engrg. 194 (9–11) (2005) 1057–1074.
[42] Z. Niu, C. Cheng, H. Zhou, Z. Hu, Analytic formulations for calculating nearly singular integrals in two-dimensional BEM, Eng. Anal. Bound. Elem. 31 (12) (2007) 949–964.
[43] Z. Han, C. Cheng, Z. Hu, Z. Niu, The semi-analytical evaluation for nearly singular integrals in isogeometric elasticity boundary element method, Eng. Anal. Bound. Elem. 95 (2018) 286–296.
[44] H. Zhou, Z. Niu, C. Cheng, Z. Guan, Analytical integral algorithm applied to boundary layer effect and thin body effect in bem for anisotropic potential problems, Comput. Struct. 86 (15–16) (2008) 1656–1671.
[45] G. Krishnasamy, F.J. Rizzo, Y. Liu, Boundary integral equations for thin bodies, Internat. J. Numer. Methods Engrg. 37 (1) (1994) 107–121.
[46] Y.J. Liu, D.M. Zhang, F.J. Rizzo, Nearly singular and hypersingular integrals in the boundary element method, WIT Trans. Model. Simul. 1 (1970).
[47] Y. Liu, Analysis of shell-like structures by the boundary element method based on 3-d elasticity: formulation and verification, Internat. J. Numer. Methods Engrg. 41 (3) (1998) 541–558.
[48] E. Lutz, Exact Gaussian quadrature methods for near-singular integrals in the boundary element method, Eng. Anal. Bound. Elem. 9 (3) (1992) 233–245.
[49] H.B. Chen, P. Lu, M.G. Huang, F.W. Williams, An effective method for finding values on and near boundaries in the elastic BEM, Comput. Struct. 69 (4) (1998) 421–431.
[50] Y. Wang, R. Qiao, H. Zhu, Particular solution method adjusted by singularity for calculating boundary stress, in: Proceedings of the Fourth China-Japan Symposium on BEM, 1991, pp. 91–102.
[51] Y.C. Wang, H.Q. Li, H.B. Chen, Y. Wu, Particular solutions method to adjust singularity for the calculation of stress and displacement at arbitrary point, Acta Mech. Sinica (1994) 02.
[52] H.B. Chen, Y.C. Wang, P. Lu, Stress rate integral equations of elastoplasticity, Acta Mech. Sinica 12 (1) (1996) 55–64.
[53] X.-W. Gao, T.G. Davies, Adaptive integration in elasto-plastic boundary element analysis, J. Chin. Inst. Eng. 23 (3) (2000) 349–356.
[54] X.-W. Gao, T.G. Davies, Boundary Element Programming in Mechanics, Cambridge University Press, 2002.
[55] M. Tanaka, V. Sladek, J. Sladek, Regularization techniques applied to boundary element methods, Appl. Mech. Rev. 47 (10) (1994) 457–499.
[56] V. Sladek, J. Sladek, Singular integrals and boundary elements, Comput. Methods Appl. Mech. Engrg. 157 (3–4) (1998) 251–266.
[57] J.F. Luo, Y.J. Liu, E.J. Berger, Analysis of two-dimensional thin structures (from micro-to nano-scales) using the boundary element method, Comput. Mech. 22 (5) (1998) 404–412.
[58] H. Ma, N. Kamiya, Domain supplemental approach to avoid boundary layer effect of BEM in elasticity, Eng. Anal. Bound. Elem. 23 (3) (1999) 281–284.
[59] H. Ma, N. Kamiya, A general algorithm for accurate computation of field variables and its derivatives near the boundary in BEM, Eng. Anal. Bound. Elem. 25 (10) (2001) 833–841.
[60] H. Ma, N. Kamiya, A general algorithm for the numerical evaluation of nearly singular boundary integrals of various orders for two-and three-dimensional elasticity, Comput. Mech. 29 (4–5) (2002) 277–288.
[61] X. Qin, J. Zhang, G. Xie, F. Zhou, G. Li, A general algorithm for the numerical evaluation of nearly singular integrals on 3D boundary element, J. Comput. Appl. Math. 235 (14) (2011) 4174–4186.
[62] J. Zhang, P. Wang, C. Lu, Y. Dong, A spherical element subdivision method for the numerical evaluation of nearly singular integrals in 3D BEM, Eng. Comput. 34 (6) (2017) 2074–2087.
[63] B.M. Johnston, P.R. Johnston, D. Elliott, A sinh transformation for evaluating two-dimensional nearly singular boundary element integrals, Internat. J. Numer. Methods Engrg. 69 (7) (2007) 1460–1479.
[64] B.M. Johnston, P.R. Johnston, D. Elliott, A new method for the numerical evaluation of nearly singular integrals on triangular elements in the 3D boundary element method, J. Comput. Appl. Math. 245 (2013) 148–161.
[65] J.H. Lv, Y. Miao, W.H. Gong, H.P. Zhu, The sinh transformation for curved elements using the general distance function, Comput. Model. Eng. Sci. 93 (2) (2013) 113–131.
[66] X. Li, Y. Zhang, Y. Gong, Y. Su, X. Gao, Use of the sinh transformation for evaluating 2D nearly singular integrals in 3D BEM, Acta Mech. 226 (9) (2015) 2873–2885.
[67] J. Lv, Y. Miao, H. Zhu, The distance sinh transformation for the numerical evaluation of nearly singular integrals over curved surface elements, Comput. Mech. 53 (2) (2014) 359–367.

[68] Y. Zhang, Y. Gong, X. Gao, Calculation of 2D nearly singular integrals over high-order geometry elements using the sinh transformation, Eng. Anal. Bound. Elem. 60 (2015) 144–153.
[69] Y. Gu, H. Gao, W. Chen, C. Zhang, A general algorithm for evaluating nearly singular integrals in anisotropic three-dimensional boundary element analysis, Comput. Methods Appl. Mech. Engrg. 308 (2016) 483–498.
[70] Y. Gu, X. He, W. Chen, C. Zhang, Analysis of three-dimensional anisotropic heat conduction problems on thin domains using an advanced boundary element method, Comput. Math. Appl. 75 (1) (2018) 33–44.
[71] Y. Zhang, Y. Gu, J.-T. Chen, Boundary element analysis of the thermal behaviour in thin-coated cutting tools, Eng. Anal. Bound. Elem. 34 (9) (2010) 775–784.
[72] G. Xie, J. Zhang, X. Qin, G. Li, New variable transformations for evaluating nearly singular integrals in 2D boundary element method, Eng. Anal. Bound. Elem. 35 (6) (2011) 811–817.
[73] G. Xie, J. Zhang, Y. Dong, C. Huang, G. Li, An improved exponential transformation for nearly singular boundary element integrals in elasticity problems, Int. J. Solids Struct. 51 (6) (2014) 1322–1329.
[74] Y.P. Gong, C.Y. Dong, Y. Bai, Evaluation of nearly singular integrals in isogeometric boundary element method, Eng. Anal. Bound. Elem. 75 (2017) 21–35.
[75] L. Piegl, W. Tiller, The NURBS Book, second ed., Springer-Verlag, Berlin, Heidelberg, 1995.
[76] T. Greville, Numerical procedures for interpolation by spline functions, J. Soc. Ind. Appl. Math. Ser. B Numer. Anal. 1 (1) (1964) 53–68.
[77] J. Trevelyan, Boundary elements for engineers: theory and applications, Comput. Mech. (1994).
[78] G.G.W. Mustoe, Advanced integration schemes over boundary elements and volume cells for two-and three-dimensional non-linear analysis, Dev. Bound. Elem. Methods 3 (1984) 213–270.
[79] S. Bu, T.G. Davies, Effective evaluation of non-singular integrals in 3D BEM, Adv. Eng. Softw. 23 (2) (1995) 121–128.
[80] Y.P. Gong, C.Y. Dong, An isogeometric boundary element method using adaptive integral method for 3D potential problems, J. Comput. Appl. Math. 319 (2017) 141–158.
[81] Y.P. Gong, C.Y. Dong, X.Y. Qu, An adaptive isogeometric boundary element method for predicting the effective thermal conductivity of steady state heterogeneity, Adv. Eng. Softw. 119 (2018) 103–115.
[82] P.R. Johnston, D. Elliott, A sinh transformation for evaluating nearly singular boundary element integrals, Internat. J. Numer. Methods Engrg. 62 (4) (2005) 564–578.
[83] D. Elliott, P.R. Johnston, The iterated sinh transformation, Internat. J. Numer. Methods Engrg. 75 (1) (2008) 43–57.
[84] Y. Gu, W. Chen, B. Zhang, W. Qu, Two general algorithms for nearly singular integrals in two dimensional anisotropic boundary element method, Comput. Mech. 53 (6) (2014) 1223–1234.
[85] S. Keuchel, N.C. Hagelstein, O. Zaleski, O. von Estorff, Evaluation of hypersingular and nearly singular integrals in the isogeometric Boundary Element Method for acoustics, Comput. Methods Appl. Mech. Engrg. 325 (2017) 488–504.
[86] T.L. Bergman, F.P. Incropera, D.P. DeWitt, A.S. Lavine, Fundamentals of Heat and Mass Transfer, John Wiley & Sons, 2011.
[87] H. Guo, H. Zhang, G. Ma, S. Gong, Thermo-physical and thermal cycling properties of plasma-sprayed $BaLa_2Ti_3O_{10}$ coating as potential thermal barrier materials, Surf. Coat. Technol. 204 (5) (2009) 691–696.
[88] R. Vaßen, M.O. Jarligo, T. Steinke, D.E. Mack, D. Stöver, Overview on advanced thermal barrier coatings, Surf. Coat. Technol. 205 (4) (2010) 938–942.
[89] M.O. Jarligo, D.E. Mack, G. Mauer, R. Vaßen, D. Stöver, Atmospheric plasma spraying of high melting temperature complex perovskites for TBC application, J. Therm. Spray Technol. 19 (1–2) (2010) 303–310.